LASER DRIVEN THIN-FILM DEPOSITION FROM FREE-FALLING PARTICLES

By

GRANT MICHAEL SCHRAG

A DISSERTATION PRESENTED TO THE GRADUATE
SCHOOL OF THE UNIVERSITY OF FLORIDA IN
PARTIAL FULFILLMENT OF THE REQUIREMENTS
FOR THE DEGREE OF DOCTOR OF PHILOSOPHY

UNIVERSITY OF FLORIDA

1987

Copyright 1987

by

Grant Michael Schrag

To my wife, Wendy and children, Erica and Amy

ACKNOWLEDGMENTS

The author wishes to express his gratitude to all who contributed to this work and to his education received at the University of Florida. In particular he wishes to thank his research director, chairman and mentor, Samuel Colgate, his co-director of research, Paul Holloway, and Dean Schoenfeld for their valuable guidance and for their individual and joint efforts which made this opportunity to work in the field of surface science possible.

Many of the author's peers have contributed greatly to this work and deserve his gratitude. Eric Lambers, who performed Auger analysis; Chris Dykstal, who did ESCA analysis; William Wresh, who recorded RBS measurements; and Oswaldo Rojas, who measured the specific surface area of the target powders. The author also wishes to thank his former labmate and longtime friend Charles Sona for his assistance and moral support throughout the years.

Finally, the author wishes to thank his committee, each of whom contributed materially to this study, the Army Research Office (ARO Grant No. DAAG29-84-K-0003) and Proctor and Gamble for their support.

TABLE OF CONTENTS

page

ACKNOWLEDGMENTS....................iv

LIST OF TABLES....................vii

LIST OF FIGURES....................viii

ABSTRACT....................xi

CHAPTERS

I INTRODUCTION....................1

II EXPERIMENTAL....................7

- Apparatus and Instrumentation....................7
  - Vacuum System....................8
  - Deposition Fixtures....................29
  - Laser and Optical System....................43
  - Auger Electron Spectroscopy System....................44
- Methods and Materials....................45
  - Power Density Determinations....................46
  - Targets and Substrates....................54
  - AES and Scanning Electron Spectroscopy....................63
  - Rutherford Backscattering Spectroscopy....................71
  - Electron Spectroscopy for Chemical Analysis....................75
  - Methods of Quantitative Analysis....................82
    - RBS determination of film stoichiometry....................82
    - Film stoichiometry from AES....................93
    - Film stoichiometry from ESCA....................95
    - Film thickness determinations....................95

III THEORY....................99

- Conventional Evaporation....................100
- Laser Evaporation....................104
- Low Temperature Laser Evaporation....................106
- High Temperature Laser Evaporation....................110
- Influence of Particle Size on Film Composition and Deposition Rate....................112

IV RESULTS AND DISCUSSION....................................116

Film Composition and Deposition Rates...............117
Film Contamination.................................126
Conclusions and Considerations for Future Work......127

APPENDIX A REDUCING APERATURE...............................132

APPENDIX B THERMOPHYSICAL DATA...............................134

APPENDIX C CLAUSIUS DERIVATION...............................139

APPENDIX D BASIC PROGRAM.....................................143

APPENDIX E MASS EVAPORATION FLUXES...........................147

REFERENCES...149

BIOGRAPHICAL SKETCH..152

LIST OF TABLES

Page

Table II.1. Operating Conditions of the Lumonics TEA 101-1 Carbon Dioxide Laser....................49

Table II.2. Power Density Determinations for Each of the Optical Schemes Used.......................53

Table IV.1. RBS Peak Areas...................................119

Table IV.2. AES Peak-to-Peak Heights from Differentiated Spectra...........................120

Table IV.3. ESCA Peak Areas..................................121

Table IV.4. Summary of Quantitative Compositional Analyses...122

Table IV.5. Calculated Film Compositions....................123

Table IV.6. Film Thickness and Deposition Rate Determinations..................................125

Table B.1. Thermophysical Data for Molybdenum................135

Table B.2. Thermophysical Data for Silicon..................136

Table B.3. Thermophysical Data for Tantalum.................137

Table B.4. Thermophysical Data for Tungsten.................138

Table E.1. Physical Properties of the Effluent Vapors for Low Temperature Laser Heating...147

Table E.2. Mass Evaporation Fluxes for Low Temperature Laser Heating as Calculated by Equations D.1. and D.2.............148

LIST OF FIGURES

Page

Fig. II.1. Completed vacuum workstation prior to installation of all other apparatus systems..9

Fig. II.2. Photograph of chamber top extention carrying sample manipulator (PM).................12

Fig. II.3. Radial distribution of vacuum chamber ports..14

Fig. II.4. Distribution of vacuum chamber ports according to level and illustrated by "rolled-out" schematic.........................16

Fig. II.5. Hybrid valve. Solid lines show valve in closed position. Phantom view shows full open position...............................20

Fig. II.6. Schematic drawing of the principal working level of the vacuum chamber showing experimental configuration.......................24

Fig. II.7. Photograph of hermetically sealed zinc selenide window. Shown disassembled............ 27

Fig. II.8. Photograph of powder curtain generating device..32

Fig. II.9. Schematic drawing showing cross-sectioned view of rotary target dispenser..................34

Fig. II.10. Drawing of the principal working level of the vacuum chamber illustrating optical scheme I...............................38

Fig. II.11. Drawing of the principal working level of the vacuum chamber illustrating optical scheme II..............................40

Fig. II.12. Drawing of sample holder..........................42

Fig. II.13. Drawing which illustrates method used to reduce laser beam diameter for energy measurements...............................48

Fig. II.14. Auger spectrum of as-inserted GaAs wafer prior to pulsed laser cleaning..............58

Fig. II.15. Auger spectrum of GaAs wafer after thirty $2Jcm^{-2}$ laser pulses........................60

Fig. II.16. Auger spectrum of GaAs wafer after 200 pulses on molybdenum-silicon mixture which immediately followed pulsed laser cleaning............................62

Fig. II.17. Auger spectrum of film deposited from molybdenum disilicide powder prior to sputter-ion cleaning.............................66

Fig. II.18. Auger spectrum of film deposited from molybdenum disilicide powder after sputter-ion cleaning.............................68

Fig. II.19. Auger compositional depth profile of molybdenum-silicide film deposited from disilicide target...........................70

Fig. II.20. Auger compositional profile as a function of beam travel across specimen..73

Fig. II.21. SEM photograph of two molybdenum disilicide residual particles. The numbers indicate points for AES Analysis...74

Fig. II.22. Rutherford backscattering spectrum. The ordinate has units of counts. The abscissa has units of energy................. 77

Fig. II.23. ESCA survey spectrum of molybdenum disilicide film prior to sputter-ion cleaning..79

Fig. II.24. ESCA survey spectrum of molybdenum disilicide film following sputter-ion cleaning..81

Fig. II.25. ESCA multiplex spectrum of molybdenum $3p_{1/2}$ and $3p_{3/2}$ transitions. (410 eV and 393 eV respectively)........................84

Fig. II.26. ESCA multiplex spectrum of molybdenum $3d_{3/2}$ and $3d_{5/2}$ transitions. (230 eV and 227 eV respectively)........................86

Fig. II.27. ESCA multiplex spectrum of silicon 2s transition (150 eV)..............................88

Fig. II.28. ESCA multiplex spectrum of silicon 2p transition (98.5 eV).............................90

Fig. II.29. Auger compositional depth profile of molybdenum disilicide film used as reference..98

Fig. III.1. Knudsen layer model of evaporation 102

Fig. III.2. Graph of mole fraction of molybdenum in film vs mole fraction of molybdenum in a target mixture with specific surface ratio as a parameter....................114

Fig. IV.1. SEM photograph of specimen mounted in the forward hemisphere along the direction of the laser beam.................................128

Fig. IV.2. SEM photograph of specimen mounted in the rearward hemisphere along the direction of the laser beam.................................129

Abstract of Dissertation Presented to the Graduate School
of the University of Florida in Partial Fulfillment of the
Requirements for the Degree of Doctor of Philosophy

LASER DRIVEN THIN-FILM DEPOSITION FROM FREE-FALLING PARTICLES

By

Grant Michael Schrag

August, 1987

Chairman: Samuel O. Colgate
Major Department: Chemistry

Thin-films of molybdenums-silicides were deposited by a new method in which mixtures of small, free-falling particles are heated by focused 10.6 micron radiation from a pulsed carbon dioxide laser in an ultra high vacuum chamber. The composition of the resulting films was adjustable and controlled by the selection of particle sizes and their relative numbers.

It was found that collecting substrates positioned in the rearward hemisphere along the direction of the laser beam were nearly free of defects. Recoil pressure exerted by the effluent vapor had the tendency to drive target residue into the forward hemisphere.

Compositional analyses of the deposited films were performed using Auger Electron Spectroscopy (AES), X-ray Photoelectron Spectroscopy (XPS) and Rutherford Backscattering Spectroscopy (RBS). The measured values of atomic concentration are consistent with surface evaporation of the particles and are in close agreement with the values calculated from the specific surface areas of the target constituents and theoretical mass evaporation rates.

Laser heating of molybdenum disilicide particles was found to produce silicon-rich molybdenum-silicon films ($x_{Mo} \leq 0.08$). Auger depth profiles of residual target particles which were collected on forward substrates were enriched in molybdenum.

CHAPTER I
INTRODUCTION

Thin films of materials may be produced by vacuum evaporation onto supporting substrates of elements and compounds using a variety of energy sources. Conventional techniques such as resistive heating, electron bombardment, and effusion from Knudsen cells have been widely used over the last 30 years.[1,2] The process of vacuum evaporation typically consists of the following distinguishable steps:[2]

1) Transition from the condensed phase to the gas phase.

2) Vapor traversing the space between the source and the substrate at reduced pressures where mass transport occurs via effusion.

3) Condensation of vapor on substrate.

When conventional techniques are applied to compounds or alloys, vapor fractionation often occurs and films containing excess amounts of the more volatile species result.[1-10] These alloys or compounds for which the vapor and condensed phases have different compositions are said to evaporate incongruently.

Whether a compound evaporates congruently or whether there exists a congruently vaporizing composition within an alloy system depends upon a rough matching of the volatilities, and hence of sublimation enthalpies of the constituents.[9]

A class of binary alloys of elements with widely different volatilities is the collection of Metal-Silicon alloys designated Metal-Silicides. Refractory Metal-Silicides are materials currently of interest in integrated circuit technology. This interest is due to two desirable physical properties common to this subclass of alloys: 1) stability at elevated temperatures; and 2) low electrical resistance.[11,12] Murarka[11] has reviewed the experimental techniques used for silicide formation. These methods include most of the techniques which have been developed to circumvent the problem of vapor fractionation:

> Silicides can be formed by sintering a thin-film metal-silicon composite deposited in one of the following ways:
>
> (i) Metal on silicon or polysilicon: metal can be deposited by sputtering, evaporation or electroplating
> (ii) Cosputtering metal and silicon on silicon, polysilicon, or oxide in a desired ratio, from two independent targets
> (iii) Cosputtering on silicon, polysilicon, or oxide from a hot-pressed silicide target
> (iv) Coevaporating on silicon, polysilicon, or oxide the elements in a two-filament or double e-gun evaporator
> (v) Chemical vapor deposition, at atmospheric or subatmospheric pressures, of the silicide on silicon, polysilicon, or oxide
>
> All these techniques of depositing films use evaporation, sputtering, or chemical vapor deposition. (pp. 115 and 116)

Of the techniques he reviewed, cosputtering of the metal and silicon from two different elemental sources was chosen by Murarka as the most favorable. The feature cited as most attractive was the ability to control the metal-to-silicon ratio in the deposit. This capability has been used to deposit alloys M_x/Si_y, with y/x changing from zero to infinity, that is, from pure metal to pure silicon.[11]

Since the development of high power commercial lasers many researchers have investigated the interaction of intense optical radiation with solids.[1-8,10,13-24] Examination of early literature in this area reveals a great interest in lasers as potential heating sources for vacuum deposition.[1-8,10] Several important advantages which laser deposition offers over conventional techniques are

(1) The laser is mounted external to the vacuum system and its beam can be highly directed at the evaporant, thus avoiding undesirable reactions and resulting in very pure films.[1-8,10]

(2) Since the heating is highly localized, the chamber may be filled with a transparent reactive gas in order to effect reactive depositions.[2,5,10]

(3) High deposition rates are obtainable without loss of good surface morphology and adhesion.[2,5,10]

(4) Laser radiation can result in congruent evaporation of some compounds which by conventional methods are difficult or impossible to deposit.[1-8,10]

(5) Crystalline films, proposedly due to the large excess kinetic energy available to condensates, frequently result even on substrates which are not heated.[2,5,10]

(6) The beam may be directed at multiple targets within the chamber, and hence used to perform supplemental tasks such as substrate cleaning, surface annealing, and target outgassing.

These advantages notwithstanding, direct laser evaporation of solids is not widely used in thin film preparation, as evidenced by Murarka's review.[11] This may be due in part to a problem with solid and molten debris typically thrown from the laser solid interaction zone.[1-8,10,13] Although this problem may be controlled in theory,[2,10,13] in practice it is difficult. Furthermore, as the study of laser evaporation of InAs by Smith and Turner[1] illustrates, congruent laser vaporization of compounds cannot be expected in every case. In that study, analysis of the deposited InAs films revealed the concentration of As contained therein was thirty-five times that of the target.

For those compounds or alloys composed of elements having extremely different volatilities (Mo-Si, Ta-Si, and W-Si alloys are a good examples) vapor fractionation and consequently non-stoichiometric films may be expected even when laser evaporation is used. Hence, a reliable method for the stoichiometric deposition of Refractory Metal Silicides is highly attractive. Such a method would have decided advantages over conventional methods, were it capable of depositing films with infinitely adjustable stoichiometric coefficients. More generally stated, an ideal vacuum deposition source would produce films which are:

1) free of both compositional impurities and debris,

2) uniform both spatially and compositionally,

3) infinitely adjustable in composition even for the most and least volatile elements and

4) produced at high rates and over large areas.

A method was postulated in which mixtures of small, free-falling particles are heated by focused 10.6 micron radiation from a pulsed carbon dioxide laser in an ultra high vacuum (uhv) chamber. The composition of the condensed films should be infinitely adjustable and controlled by proper selection of the particle sizes and relative numbers. A widely accepted model for laser-solid interaction suggests that the relative surface areas of the particles exposed to the laser beam would be a principal factor effecting film composition. This model assumes that sublimation of the solid occurs via quasi-stationary surface ablation when the laser pulse duration is less than 1 millisecond and the absorbed energy density exceeds a certain minimum amount specific for each element.[14-22]

Secondly, the use of small free-falling particles as targets would enhance the chance for defect free films. It has been observed that when pulsed laser radiation is focused on the surface of a massive target, a plume of vaporized (indeed partially ionized) material is ejected. The plume geometry is independent of the angle of incidence of the beam and always normal to the surface of the solid. Thus the recoil pressure exerted by effluent vapor (as in rocket propulsion) would have the tendency to drive any microscopic target particles not totally evaporated in the forward hemisphere along the direction of the beam. If the collecting substrate were positioned in the rearward hemisphere, few if any debris particles would contaminate the films produced.

An apparatus was designed and fabricated for testing these postulates. The results of that research are presented in the following chapters.

CHAPTER II
EXPERIMENTAL

Apparatus and Instrumentation

The evaporation of thin films with controlled properties requires an operating environment which interferes as little as possible with the process of film formation. The mechanism of vapor transport, the substrate impingement rate and the film purity are all influenced by the total pressure of the system.[2,25-27] In the range of pressures commonly termed Very High Vacuum (VHV; $10^{-6} > p > 10^{-9}$ torr) the number of collisions of the condensing vapor with the substrate (assuming an equilibrium velocity distribution) is sufficient for reasonable deposition rates and hence adequate to deposit many films. The nature and concentration of residual gases in the deposition environment are equally important considerations. At 10^{-6} torr the time necessary for surface coverage by a monolayer of background gas is approximately one second. Pressures below 10^{-8} torr (uhv) are necessary to ensure clean surface conditions and high film purity.[26,27]

So as to minimize film contamination and to enable in situ compositional analysis of the deposited films (by Auger Electron Spectroscopy (AES)), the deposition vessel was designed and constructed using standard uhv practices.

The laser deposition apparatus was composed from four principal elements: 1) the uhv system; 2) the deposition fixtures (i.e. special target and substrate holders); 3) the laser and optical system; and 4) the AES system. It is within the vacuum chamber that all system elements interact and where all materials processing is performed. Thus, it is appropriate that the vacuum system be the first experimental element described.

Vacuum System

For ease in location near and alignment with the laser system, the vacuum system was designed and constructed to function as part of a mobile experimental station (fig. II.1.). It is comprised of a welded supporting frame, a uhv chamber, a turbomolecular pump, a backing mechanical pump, a titanium sublimation pump, a helium mass spectrometer leak detector, the vacuum foreline connections, the power supplies and the controllers.

The supporting frame, which is the basis of the workstation, was constructed from 3 in. X 3/8 in. structural aluminum angle. Castors and leveling feet were located at each corner. It is capable of furnishing both space and support for all vacuum system elements and includes a vibrationally isolated optical table, a working surface and storage facilities for vacuum hardware and handtools.

High temperature processing is a necessity if ultrahigh

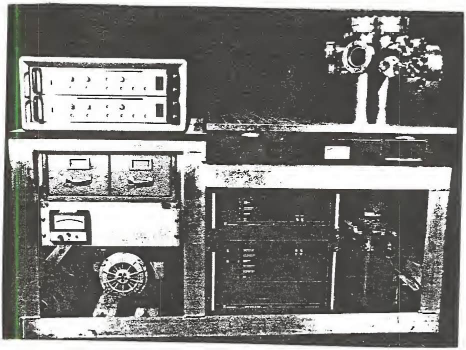

Fig. II.1. Completed vacuum workstation prior to installation of all other apparatus systems

vacuum is to be attained after a reasonable pumping time.[25] The materials, fabrication techniques, and seals used for the construction of the chamber walls and internal fixturing were thus chosen for their compatibility with thermal cycling. The welded, all metal vessel was fabricated entirely from type 304 stainless steel (304-SST). The chamber body is a cylinder 14 in. high with an outside diameter of 8.6 in. (8.4 in. i.d.). The vacuum flanges were made from plate stock and, with two exceptions, machined to conform to standard conflat (CF) dimensions. It should be noted that the o.d. of the chamber body is oversized for use with standard CF flanges. Thus the chamber top (10 in. o.d. CF) was bored fully to the inside dimension of the knife edge. The chamber bottom (8 in. o.d. CF), to which a turbomolecular pump was mounted, was built having blind-tapped holes and an outside diameter equal to the inside diameter of the chamber (8.4 in. o.d.). These modifications allowed for maximum conductance as well as maximum space for sidearm openings.

A top extension (6 in. o.d. CF), carrying a sample manipulator (PM; fig. II.2.), was mounted eccentrically to the chamber top. The radial displacement of the center of motion for the manipulator from the center of the chamber was one-half the inside radius of the chamber. The angle of its position could be varied from 0° to 360° in increments of 15° (corresponding to the 24 hole bolt pattern of the top flange).

The chamber sidearms were located on three levels. Their arrangement (figs. II.3. and II.4.) was chosen on the basis that it would include an adequate number of each of the varied sizes

Fig. II.2 Photograph of chamber top extension carrying sample manipulator (PM)

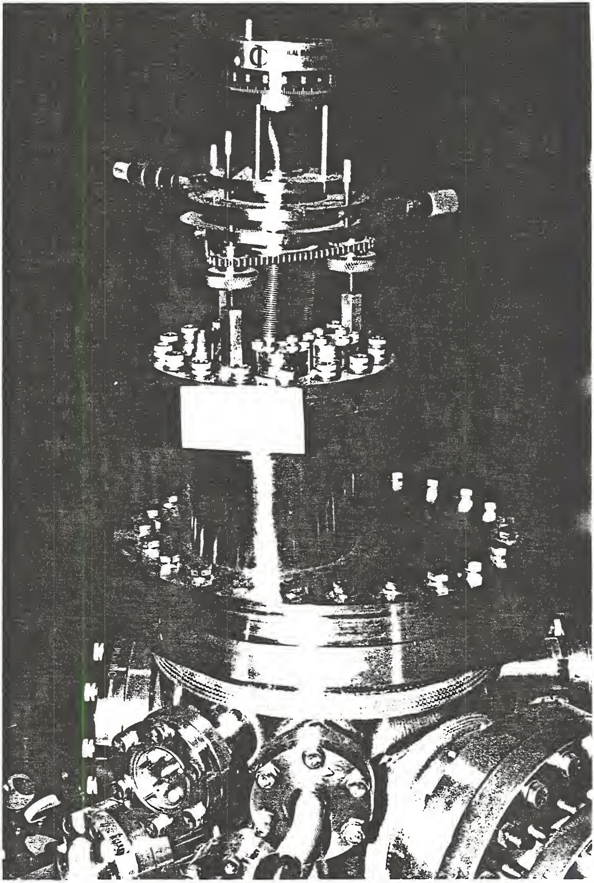

Fig. 11.3. Radial distribution of vacuum chamber ports

RT- Rotary target feedthrough
LD- Leak detector valve
AC- Auger cylindrical mirror analyser
SH- Hinged shutter to cover CMA
AG- Argon sputter-ion gun
IG- Nude ionization gauge
ZS- Zinc selenide window
GV- Glass viewport
QW- Quartz window
TS- Titanium sublimation filament
VV- Varian leak valve

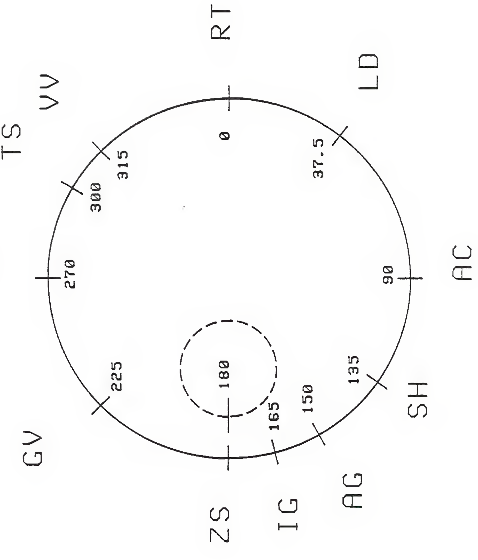
RT
0
LD
37.5
AC
90
SH
135
150
AG
165
IG
180
ZS
GV
225
QW
270
300
315
TS
VV

Fig. II.4. Distribution of vacuum chamber ports according to level and illustrated by "rolled-out" schematic

Level I- Topmost level (utility)

LD- Leak detector valve
SH- Hinged shutter
IG- Nude ionization gauge
TS- Titanium sublimation filament

Level II- Middle level (viewing)

GV- Glass viewport

Level III- Lowest level (Experimental)

RT- Rotary target feedthrough
AC- Auger cylindrical mirror analyser
AG- Argon sputter-ion gun
ZS- Zinc selenide window
QW- Quartz window
VV- Varian leak valve

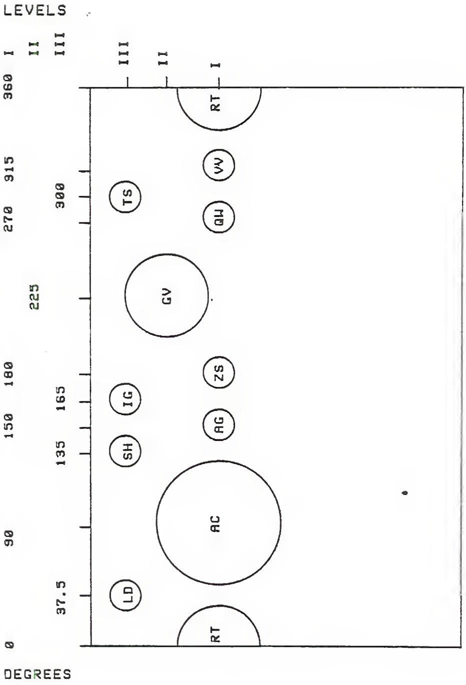
LEVELS
I
II
III
III
II
I
360
315
270
300
225
180
165
150
135
90
37.5
0
DEGREES
RT
VW
TS
QW
GV
ZS
IG
AG
SH
AC
LD
RT

of flanges in order to accommodate the foreseeable experimental needs; assure easy access for handtools and fasteners; provide space for future additions; allow for a maximum viewing angle from the viewport (GV); and orient principal ports opposite each of the laser windows (QW and ZS).

The uppermost level (III, fig.II.3) with four rotatable 2.75 in. CF sidearms was designed as a utility level. Their functions in the ultimate experimental configuration were as follows: a port (LD) for communication with a helium mass spectrometer leak detector; a port (SH) for operation of a hinged shutter mounted on a rotary bellows feedthrough; a port (IG) for a nude ionization gauge; and a port (TS) for a titanium sublimation pump (TSP) filament.

A novel uhv vacuum valve[28] was constructed in order to incorporate an NRC Equipment Corporation, model NRC 925, mass spectrometer leak detector (as commercially available valves were inappropriate for this application). The valve employed a hybrid of two vacuum sealing techniques--elastomeric O-rings and soft metal gaskets--in contrast to commercially available valves, where one or the other sealing technique is used exclusively. This design maintained the singular advantage of an all metal vacuum valve, its ability to withstand high temperature bakeout, while it eliminated the expense and complexity of bellows construction. While construction simplicity and convenient usage were considered to be key design factors, the frequency of use and conditions of the vacuum during the time the valve would be open were also design factors.

The stem and body of the valve were constructed entirely from 304-SST. The body of the valve (fig. II.5.) was constructed from a 1.5 in. o.d. tee (T) to which a 2.75 in. o.d. bonnet sealing flange (F) and a 2.75 in. o.d. CF chamber mating flange (C) were TIG welded. The valve seat was designed to be compatible with 1.33 in. o.d. CF gaskets. Half of this gland (G) is incorporated with the chamber mating flange which was constructed from a double sided (2.75 in.-1.33 in.o.d.) CF flange. The remaining half of the CF gland which comprises the valve seat was machined onto the stem plunger (P). On the plunger face, a hole was tapped for a 6-32 allen cap screw which may be used, along with a tapered bushing (H) to hold a standard "mini" CF gasket in position for sealing. The forward face of the plunger was champhered at 45° to facilitate motion of the valve stem assembly. The plunger was attached to the valve stem (S) by a retaining ring and ball bearing assembly. The retaining ring (R) restrains a Fafnir KS4 self-aligning ball bearing (A) which was pressed onto a 0.25 in. diameter shoulder of the valve stem. The valve stem was sealed to the bonnet by a reciprocating O-ring seal and was threaded with a right-handed 5/8-8 acme thread for closure of the valve seat. The bonnet (B) was sealed to the mating flange on the valve body using a viton O-ring face seal. The valve sidearm was reduced to 1 in. o.d. by brazing an appropriately sized reducing bushing. The NRC Equipment Corporation mass spectrometer detector head was then mounted to the sidearm using a viton quick-connect seal.

Fig. II.5. Hybrid valve. Solid lines show valve in closed position. Phantom view shows full open position

T- 1.5 in. o.d. tee
F- Bonnet sealing flange
C- Chamber mating flange
G- Ultra-high vacuum side of valve seat
P- Stem plunger
S- Valve stem
R- Retaining ring
A- Self-aligning ball bearing
B- Valve bonnet

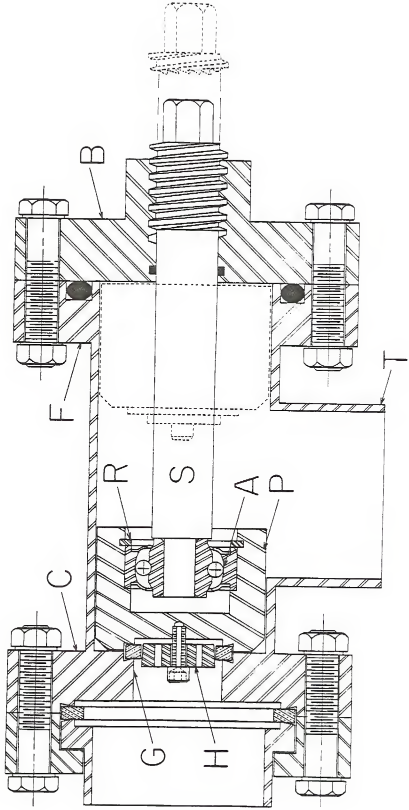
B
F
T
R
S
A
P
C
G
H

The valve was operated manually by applying torque in the appropriate direction (clockwise for closure). After several closures the gaskets could be serviced by removal of the bonnet and stem assembly.

For maximum conductance, the plunger could be drawn fully past the sidearm (as shown by a phantom view in figure II.5.). This was achieved by disengaging the threaded stem from the bonnet.

The utility of this valve has been demonstrated on several occasions--having been used not only for leak detection but also for venting with nitrogen and rough pumping the chamber.

A hinged shutter was fabricated by folding 304-SST sheet metal. Its overall dimensions were such that it could be inserted through the sidearm (SH; figs. II.3 and II.4). The shutter was hung freely on loop formed in a 0.062 in. 304-SST rod. The rod which was brazed to a stainless steel spring clip was then attached to the shaft of a rotary bellows feedthrough The shutter was used to cover the opening of a cylindrical mirror analyzer which is part of the AES system.

The ion gauge installed in port, IG, was a Dual Tungsten Filament Nude Ionization gauge, Granville-Phillips model number 274 022. Filaments were replaced as needed by spotwelding 0.007 in. diameter tungsten wire helices in place of the original tungsten filaments. These replacement filaments were manufactured by winding approximately fourteen turns of the tungsten wire around a number 60 drill blank. The resulting coil was then stretched to match the length of the original filament. Pressure measurements taken with the replacement filaments, when using the same ionization gauge controller, were found to be virtually identical to those taken using commercial filaments. The chamber pressure was continously monitored using a Nucor model VMV-400 Ionization Gauge Controller.

A Varian TSP cartridge, model 916-0017, was modified to fit within the limited space between the top of the vacuum chamber and the principal working level. This modificaiton consisted of shortening the standard ground rod and one filament and fabricating a 90° rod clamp. The filament, positioned tangentially to the chamber wall, was shielded from the remainder of the chamber interior by a mask which was fabricated from 304-SST sheet. The mask and exposed walls thus defined the effective pumping surface area. Due to this peculiar geometry, the installation and filament replacement could be made only by removing the chamber top.

The middle level (level II, figs. II.3. and II.4.) was specifically designed for viewing the inside of the chamber. For reasons of safety, the only port on this level (GV; 4-5/8 in. CF) was located in a position such that direct viewing of either laser window would be impossible. An MDC Manufacturing Inc. zero length glass viewport was subsequently installed in this position.

The lowest level (level I; fig. II.6.) was designed to function as the principal experimental level. Included on this

Fig. II.6. Schematic drawing of the principal working level of the vacuum chamber showing experimental configuration

RT- Rotary target feedthrough
CA- Cylindrical mirror analyser
AG- Argon sputter-ion gun
ZS- Zinc selenide
QW- Quartz window
VV- Varian leak valve

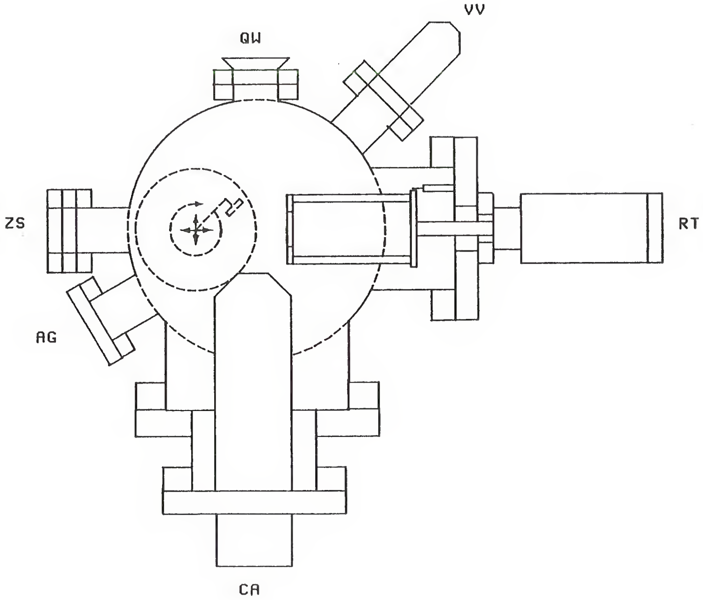
VV
QW
ZS
RT
AG
CA

level were four 2.75 in. o.d. CF ports, a 6 in. od. CF port (RT) and an 8 in. o.d. CF port (AC).

To one of the smaller ports (VV) a Varian Variable Leak Valve, model 951-5106, was mounted. Its function was to provide a means for introducing the sputtering gas necessary for the operation of a Physical Electronics Sputter Ion Gun, model 04-161, which was also installed via one of the small sidearm ports (AG).

The remaining 2.75 in. CF ports were used for mounting laser windows. Port (QW) was specifically designed for use with a quartz window. Its short length was intended to provide the maximum possible angle of incidence between the incident laser beam and window. Quartz was selected as a window material for its visible transmission characteristics. The 2 in. diameter quartz window used was obtained from MDC manufacturing Inc. mounted on a 2.75 in. o.d. CF flange. A Zinc Selenide window was mounted on port (ZS). As hermetically sealed infrared windows are not commercially available, it was necessary to custom build one. A 2.0 in. o.d. infrared window, coated for maximum transmission at 10.6 microns, was obtained from II-VI Inc. This window was mounted to a modified 2.75 in. o.d. CF flange (fig. II.7.) which could then be mated to the chamber. The window is sealed on each face by a viton O-ring and is retained by an aluminum spider.

Directly opposite the Quartz window, and on the same level, a Physical Electronics, model 10-150, cylindrical mirror analyzer was mounted (AC, figs. II.3.-II.5.). The quartz window could thus be used for accurately positioning of the specimen in front of the CMA.

Fig. II.7. Photograph of hermetically sealed zinc selenide window. Shown disassembled

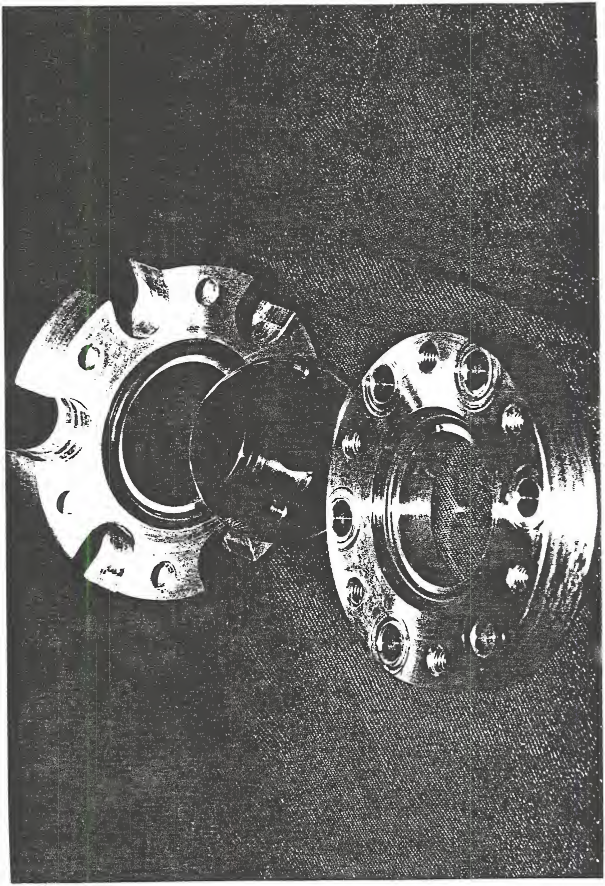

The target fixture (described in the next section) was mounted on a Huntington rotary motion feedthrough, model VF-166. This was installed in the 6 in. o.d. CF port (RT) which is located directly opposite the infrared laser window (ZS). As the Huntington feedthrough was intended for mating with a 2.75 in. o.d. CF flange, it too was modified by using a double sided 6 in.- 2.75 in. o.d. CF adapter flange. The purpose of this somewhat awkward arrangement was to enable the insertion of a reasonably sized target fixture.

The vacuum chamber and turbomolecular pump were supported by the 1 in. thick aluminum optical table of the workstation. The vacuum system was assembled through a bored 8.05 in. hole in the table. The vacuum vessel was retained by an 8.65 diameter, 0.5 in. deep, circular step concentric with this hole. The pump, mounted, below the table, was attached to the bottom of the chamber using nuts and appropriately sized lengths of treaded rod ("studs") in lieu of bolts.

Evacuation of the vessel was accomplished using a Leybold-Heraus, model TMP 560 M, turbomolecular pumping system and the modified Varian TSP (descibed above). The TSP was operated using a Varian Titanium Sublimation Pump Controller, model 922-0032. The TMP 560 system fully described includes the Leybold-Heraus Turbotronik frequency converter, model NT 560 M; Magnetronik power supply, model NT 560 M; and the Trivac mechanical backing pump, model D30A. The backing pump is connected to the turbomolecular pump by means of segmented, 1.5 in. i.d. foreline.

Contained in the foreline were a Leybold-Heraus DN40KF adsorbtion trap filled with activated alumina adsorbent to reduce hydrocarbon back-streaming; a Varian model 1254 electro-pneumatic high vacuum valve to prevent backflow from the mechanical pump in the event of power failure; a Leybold-Heraus venting valve and tee and an MDC Manufacturing Inc. TGT-1518 thermocouple gauge tube. The foreline pressure was monitored using an MDC Manufacturing Inc. TCC-210 thermocouple gauge controller. The backing pump, also mounted on the workstation, was vibrationally isolated from the chamber and optical table by three forms of isolation. First, the pump base was attached to the aluminum frame using composite flexible supports of wood and rubber. Second, the foreline between the mechanical and TMP pump contained two perpendicular flexible metal hoses. And third, the optical table supporting both the chamber and TMP was mounted on an Ealing pneumatic vibration isolation yoke, model 24-6314.

Deposition Fixtures

In order to create a target of intimately mixed free falling particles, a rotary powder dispenser was constructed. It was designed to provide a thin curtain of powder and to collect any unevaporated or partially evaporated particles which could then be redispensed. While a variety of flash evaporation mechanisms which create streams of free falling powders have been previously constructed,[2] they are significantly different from the mechanism which was fabricated for laser evaporation. The fundamental reason for these differences is that the method of flash evaporation presupposes total evaporation of the particles. The powder curtain generator (fig. II.8.), fabricated entirely from 304-SST, was constructed on two 0.25 in dia. supporting rods which were drilled and tapped at both ends. The rotary powder dispenser and a ratchet assembly mounted on opposite ends of these rods were fastened to them by machine screws which threaded into the tapped holes. A utility mounting ring which could slide on the supporting rods was mounted directed behind the powder dispenser. The position of the ring could be fixed relative to the powder dispenser by means of allen set screws.

The rotary target dispenser (fig. II.9.) consisted of two identical, radially symmetic halves (P). When assembled these machined plates defined a circular cavity. A cross sectional view of this cavity resembles two coaxially mounted hourglasses. An eight hole bolt circle was used to fasten the two halves. Located inside the bolt circle was an annular cavity which contained a circular auger. This auger (A), a flat helix with the ends joined to form a continuous loop, was fabricated from a 0.125 in. diameter stainless steel curl which was produced by making a face cut on bar stock with a lathe tool. The annular cavity was intersected by an outer vee groove. The intersection of the outer (OV) and inner (IV) 30° vee grooves defines a pair of opposing, circular knife edges which were separated by 0.005 in. The resulting slit (S) determined the overall width of the powder curtain.

Fig. II.8. Photograph of powder curtain generating device

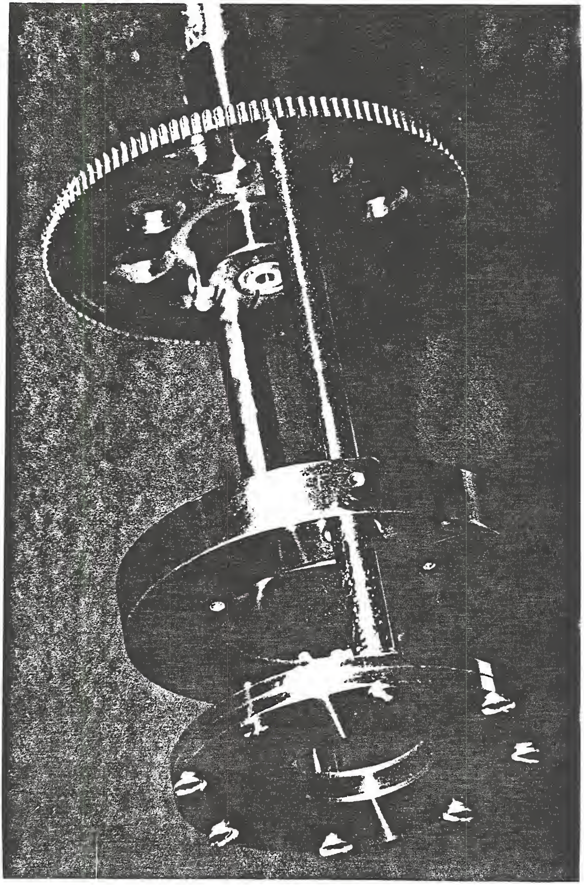

Fig. II.9. Schematic drawing showing cross-sectioned view of rotary target dispenser

P- Mating halves of target dispenser
A- Circular auger
S- Slit which defines width of powder curtain
IV- Inner vee groove
OV- Outer vee groove

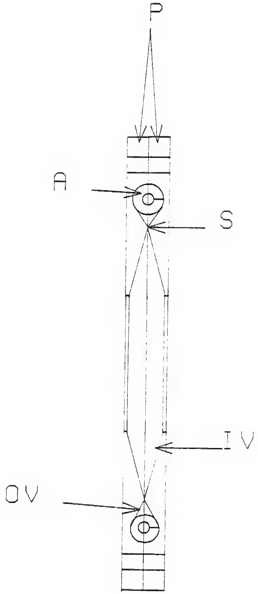
P
A
S
IV
OV

The ratchet assembly consisted of a 2.5 in. dia. fine-toothed gear which was engaged with a light weight stainless steel leaf spring. The leaf spring was mounted on the end of 0.25 in. dia. rod which, in turn, was threaded into a blind tapped hole in the supporting CF flange. The gear was attached by means of a gear clamp to a 0.25 in. dia. step machined onto an adapter fitting. This fitting was then slipped over and fastened with allen set screws to the 0.375 in. dia. shaft of a Huntington VF-166 rotary motion feedthrough. The rotation of the gear against the leaf spring created a rapid, intermittent pause in the motion of the powder dispenser. The resulting shaking motion greatly assisted the flow of powder through the dispenser slit.

A mounting ring was designed to accommodate concave gold front surface mirrors. A 2.25 in. o.d. stainless steel ring contained a stepped hole. The diameter of the inner step was 0.032 in. smaller than the outside diameter of the mirrors (1.0 in.). The outer step was machined 0.001 in. larger than the outside diameter of the mirrors. Outside the outer step, three equally spaced, tapped holes were provided for fastening a mirror retaining ring.

In addition to providing support for a reflecting element, the ring served as a convenient site for mounting substrates. If they extended beyond the front surface of the mounting ring, the screws used to fasten the retaining ring could also be used for fastening samples to the powder curtain generator.

A sample manipulator (PM; fig. II.2) was needed which would be capable of positioning the substrate to be coated in four distinct locations within the chamber while not interfering with the passage of the laser beam. One position (S1; figs. II.10. and II.11) was used for deposition. A second position (S2) was used for in situ AES analysis. A third position (S3) was used to clean the surface, prior to deposition, using pulsed 10.6 micron laser radiation. And a fourth position (S4) was intended for substrate cleaning, by ion bombardment, using an argon sputter-ion gun.

A Physical Electronics 10-504 manipulator, to which a specifically designed sample holder was affixed, was modified accordingly. The manipulator shaft (MS; fig. II.12.) could be translated along three mutually perpendicular axes. The shaft was freely rotatable and could be tilted in two directions. Two modifications were performed on the manipulator itself. First a vernier scale was added to increase the angular position accuracy from the nearest 2° to the nearest 0.2°. And second the shaft was lengthened to provide for the maximum vertical travel of the sample holder in the vicinity of the principal experimental level.

An all 304-SST sample holder (SH; fig. II.12.) was built. Four equally spaced tapped holes were located at the corners of the square holder. Two berylium-copper clips (BC) were attached to the holder using the uppermost pair of holes. These clips and two additional machine screws, located in the bottom pair of holes, served to secure samples to the front surface. The holder was supported from one end of a ductile 0.062 in. wire (SW). The

Fig. II.10. Drawing of the principal working level of the vacuum chamber illustrating optical scheme I

GM- Front surface gold mirror
GL- 200 mm focal length germanium lens
S1- Position of sample during deposition
S2- Position of sample during AES analysis
S3- Position of sample during pulsed laser cleaning
S4- Position of sample for argon-ion sputtering

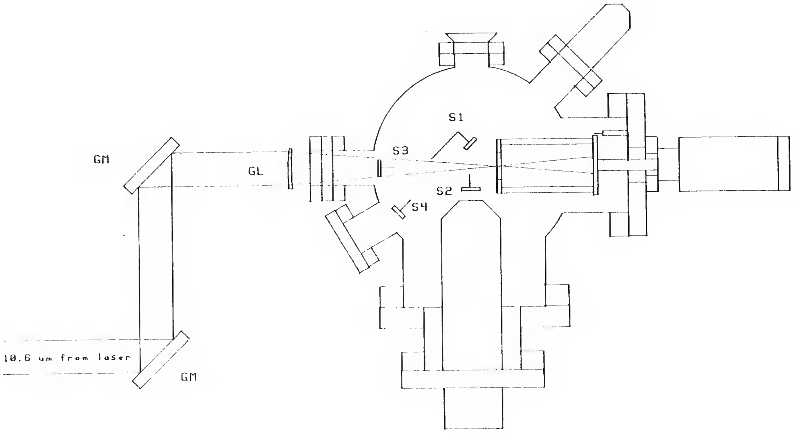
S1
GM
S3
GL
S2
S4
10.6 um from laser
GM

Fig. II.11. Drawing of the principal working level of the vacuum chamber illustrating optical scheme II

GM- Front surface gold mirror
MA- Thermal paper mask
FM- Internally mounted focusing mirror (-25 mm)
RS- Position of rear mounted specimens
S1- Position of sample during depositions
S2- Position of sample during AES analysis
S3- Position of sample during pulsed laser cleaning
S4- Position of sample for argon ion sputtering

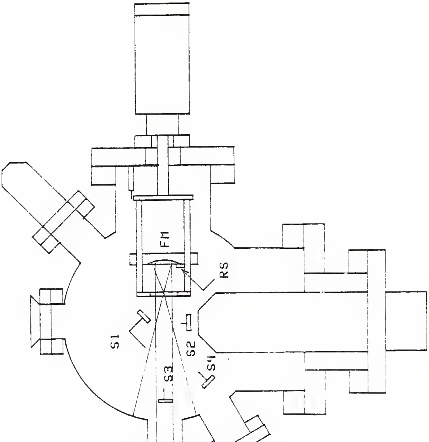
FM
RS
S1
S2
S3
S4
MA
GM
GM
10.6 um from laser

Fig. II.12. Drawing of sample holder

MS- Physical Electronics sample manipulator shaft
RH- Rod-like specimen holder
SW- Formed stainless steel wire
SH- Sample holder
BC- Berrylium-copper spring clips

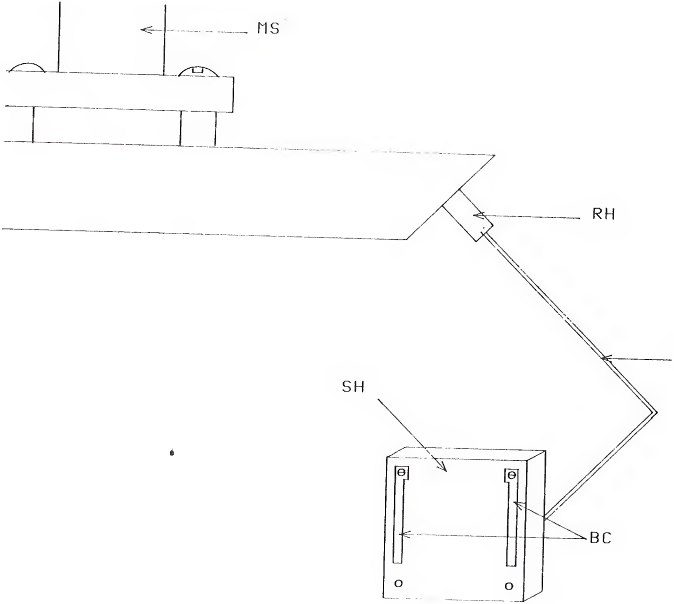
MS
RH
SW
SH
BC

opposite end was joined to a 0.125 in. bushing which could be rigidly held by the original rod-specimen holder (DH). A model of the internal structure of the vacuum chamber (at the principal level) was constructed for use as a fixture. The fixture was mounted on the bed of a milling machine; and, the shaft extension with the affixed sample holder was then mounted in the machine spindle. The support wire was then bent in such a way that the normal to the surface of the sample holder was perpendicular to the manipulator shaft; the front surface of a typical sample fastened to the holder was at the focal point of the CMA electron beam when the manipulator was at its center of travel; the holder could be rotated through 360°; and no part of the manipulator structure interfered with the passage of the laser beam when the holder was in position for deposition.

Laser and Optical System

The laser used for the experiments described below was a Lumonics TEA-101-1 pulsed carbon dioxide laser. The maximum optical pulse energy obtainable was 2.5 J. The pulse energy was varied by adjusting the operating voltage and gas mixture. The optical pulse half-width was 250 nsec. The emitted wavelength, corresponding to the P(20) line in the 001-100 band, was 10.6 microns. The laser could be fired at a repetition rate of 1 pulse per second.

The output laser beam was directed into the vacuum chamber through the chamber's zinc selenide window using two flat front surface gold mirrors, Edmund Scientific model E32,435. The mirrors were mounted using model 600A-2 Newport Research Corporation mirror mounts parallel to each other and at 45° degree angles to the laser beam.

Two focusing methods, and hence two optical arrangements, were used in these experiments. The first optical scheme (fig. II.10.) used an externally mounted meniscus lens (GL; 200 mm focal length). The lens, Oriel model 4365, was coated with an anti-reflection coating for maximum transmission at 10.6 microns. The second system (fig. II.11.) employed an internally mounted concave focusing mirror (FM; 25 mm focal length). The front surface gold mirror, Edmund Scientific model E41,806, was positioned within the chamber, using the mounting ring of the powder curtain generator, at a 0° angle of incidence with the laser beam. To prevent film contamination, arising from laser interaction with the front surface of the rotary powder dispenser, the laser beam was partially masked. The mask (MA) was fashioned from thermal printer paper. The restricting aperture was only slightly smaller than the diameter of rotary powder dispenser opening.

Auger Electron Spectroscopy System

In situ AES was performed using a Perkin Elmer 10-150 cylindrical-Auger electron optics system, 11-500 Auger system control, and a rebuilt 18-010 electron gun control. The Auger signals were amplified using an EG&G model 5101 lock-in amplifier. Primary electron beam voltage was supplied by a Fluke 410B DC high voltage power supply. The electron multiplier voltage was supplied by a Keithley Instruments Inc. model 246 high voltage supply. The spectra from this system were recorded on a Hewlett-Packard 7035-B XY recorder.

Methods and Materials

In the previous section the principal elements of the experimental apparatus used in this study were described in detail. In this section the experimental description is enlarged to include both the methodology and materials selections. In each case studied thin films were deposited by vacuum evaporation of small, free-falling particles. The particles were heated by pulses of focused 10.6 micron radiation emitted by a TEA carbon dioxide laser.

The molybdenum disilicide phase of the molybdenum-silicon binary system was specifically selected for study for the following three reasons: 1) All phases of the molybdenum-silicon system are known to evaporate incongruently when conventional heat sources are employed. 2) Refractory metal silicide thin films are of considerable current interest to integrated circuit technology. 3) Molybdenum disilicide films, which had been previously characterized,[29,30] were available for reference and comparison. The composition of the target particles, the arrangement of the substrates (relative to the source) and the incident power density on the target were all varied. The resulting films were analyzed using scanning electron microscopy (SEM); Auger electron spectroscopy (AES); X-ray photoelectron spectroscopy (XPS, also known as electron spectroscopy for chemical analysis or ESCA); and Rutherford backscattering spectroscopy (RBS). In some cases the molybdenum disilicide films obtained from J. K. Truman and P. H. Holloway[29,30] were used as chemical and physical standards. For example, rates for sputtering molybdenum silicides, when using a particular sputter-ion gun for film thickness determinations, were calibrated using the time observed for removal a previously prepared and characterized 1000 Å disilicide film. In other cases these films were used simply for qualitative comparison such as in microscopic examination of film defects.

Power Density Determinations

The laser beam energy output for each set of operating conditions used was measured and is listed in Table II.1. The laser output energies were measured using a Scientech model 138102 volume-type laser calorimeter and a Scientech 365 laser power/energy meter. As the unfocused beam diameter exceeded the aperture size of the calorimeter, a -1.0m concave focusing mirror

Fig. II.13. Drawing which illustrates method used to reduce laser beam diameter for energy measurements

SC- Scientech 138102 volume-type laser calorimeter
SM- Scientech 365 laser power/energy meter
GM- Front surface flat gold mirror
FM- Focusing mirror (-1.0 m focal length) gold front surface mirror

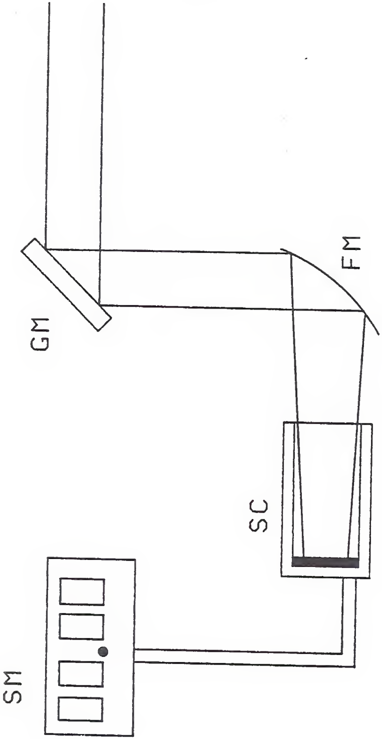
GM
FM
SC
SM

Table II.1. Operating Conditions of the Lumonics TEA 101-1 Carbon Dioxide Laser

Laser Settings	I	II	III
Operating Voltage (kilovolts)	30	37	40
Spark Gap Pressure (psig)	12	18	21
Nitrogen Flow Spark Gap (SCFH)	1.0	1.0	1.0
Nitrogen Flow Laser Tube (SCFH)	0.4	0.6	1.0
CO_2 Flow Laser Tube (SCFH)	2.0	2.0	2.0
Helium Flow Laser Tube (SCFH)	8.0	7.0	7.0
Energy Output (Joules)	1.8	2.2	2.5

was used to reduce the beam diameter. Consideration was made for the fact that reflective losses from two optical surfaces are included in these measurements and that in the actual experiment two flat mirrors (GM; figs. II.11. and II.12.) obtained from Edmund Scientific were used to direct the beam into the chamber. According to data supplied by manufacturers of the optical components used in these experiments, reflective losses for each surface would not have exceeded 1.5%. Hence, the substitution of this Oriel model 4521 concave mirror for one of those previously described would not have changed the incident energy on the target from that measured in the calorimeter. The reflective losses from the remaining optical surfaces ($\wp$) were then estimated as 1.5% from each surface, and the fraction of energy arriving at the target (ϕ_L) was calculated as

$$\phi_L = (1-\wp)^n \qquad \text{II.1.}$$

where n is the number of such surfaces in the optical scheme unaccounted for in the energy measurement. The energy incident on the target was thus calculated as follows:

$$\epsilon_I = \epsilon_I^o \cdot \phi_L \cdot (1-\phi_A) \qquad \text{II.2.}$$

where ϵ_I is the calculated incident energy, and ϵ_I^o is the energy measured by the Scientech calorimeter. The factor ϕ_A is the estimated energy lost due to the reducing aperture (MA; fig. II.11.) used in optical scheme II ($\phi_A = 0$ for optical scheme I; Appendix A).

The diameter of the laser beam at the coincidence point with the target was estimated for each of the optical schemes (figs. II.10. and II.11.) used in these experiments. It is this spot size which was most significant in determining the energy flux, energy density and power density in these experiments. To estimate this value for scheme I, a 0.080 in. thick copper sheet was placed within the vacuum chamber at the focal point of the 200 mm germanium lens. The copper was then irradiated by a succession of focused laser pulses until the resultant crater had penetrated the back-side of the target. The exit hole was then measured using a metallurgical microscope and found to be in agreement with the value calculated for a diffraction limited spot. It was thus reasoned that no significant abberations existed and the spot size could be estimated from geometric arguments with little error.

Whereas the focal length (200 mm) of the germanium lens used in scheme I was less than the shortest possible distance between the lens and the rotary powder dispenser, the beam was only partially focused at the plane of the powder curtain. The effective spot size was estimated using the difference (x) between the measured separation of the lens and target and the focal length of the lens:

$$(d_s/2)/x = (\varphi_B/2)/f \qquad \text{II.3.}$$

This relationship, which may be easily derived using the principle of corresponding triangles, relates the effective spot size (d_s) to the diameter of the unfocused beam (φ_B) and the focal length of the germanium lens (f).

The spot size for optical scheme II was estimated by assuming diffraction limited performance of the concave focusing mirror (FM; fig. II.11.). The minimum spot size for a diffraction limited element was calculated as follows:

$$d_s/2 = (4/3)\cdot\pi\lambda\cdot(f/\varphi_B) \qquad \text{III.4.}$$

where (λ) is the wavelength (in this case φ_B was taken to be the diameter of the reducing aperture, MA; fig. II.11.).

The incident energy density (J_I) for each optical scheme could thus be estimated from the relation

$$J_I = \epsilon_I/\{\pi(d_s/2)^2\} \qquad \text{II.5.}$$

using the values obtained from equations II.2.-II.4.

The incident power density (q_1), which is ultimately the parameter of importance for laser heating, was calculated from the energy density and pulse duration (τ_p).

$$q_1 = J_I/\tau_p \qquad \text{II.6.}$$

The values of power density, energy density, focal diameter and beam energy are tabulated for each optical scheme in table II.2.

Table II.2. Power Density Determinations for Each of the Optical Schemes Used.

Optical Scheme	I	II
Measured energy output (joules)	2.5	1.8
Percent transmittance	0.94	0.40
Incident energy (joules)	2.35	0.72
Beam diameter at coincidence (microns)	1500	100
Energy density (joules/cm^2)	33	9200
Pulse duration (nanoseconds)	250	250
Power density (Megawatts/cm^2)	130	37000

Targets and Substrates

Molybdenum, silicon and molybdenum-silicide films were prepared by pulsed laser evaporation of free falling powdered solids. The molybdenum-silicide films were deposited both from mixtures of elemental particles and from molybdenum disilicide powder. The size distribution of the powder types differed, but the mean particle diameter for each was less than 10 μm.

The molybdenum powder used in these experiments was obtained from Johnson-Matthey Inc. (Aesar, cat. #10030) with a reported purity of 99.9%. The particle size range was 3-7 μm in diameter. The true powder density and the specific surface area were determined to be 10.2 g/cm^3 and 0.300 m^2/g respectively.[2]

The silicon powder, supplied by Dr. M.D. Sacks (U.F. Department of Materials Science and Engineering) and previously characterized,[31] was a ground silicon powder of 0.2-10 μm in diameter. The true powder density was 2.35 g/cm^3 and its specific surface area was 4.8 m^2/g.

Molybdenum-silicon powder mixtures of two compositions were prepared using gravimetric methods. Samples from each of the elemental sources described above were dried and then weighed to the nearest tenth of a milligram, on a Sartorius analytical balance, using the same tare. The mole fractions of molybdenum in the target mixtures ($X_{Mo,T}$) were 0.33 and 0.69.

Molybdenum disilicide (Alfa cat. #48108, lot #110381) was obtained at 99.9 % purity. The mole fraction of molybdenum in the target was thus 0.33. Density and specific surface area values were not available and were not determined. Particle diameters were measured using a metallurgical microscope and were determined to be less than 10 μm. Whereas the relative surface areas of molybdenum and silicon were the same in this specimen, no further attempts to characterize the particle size distribution were made.

The number, type and orientation of supporting substrates also varied from one experiment to another. Films were deposited on either glass, carbon, silicon or gallium arsenide. The substrate materials for each experiment were intentionally selected for their compatibility with specific methods of thin film characterization. To facilitate AES identification of film impurities, single crystal semiconductor wafers were used for elemental film depositions. Molybdenum films were prepared on silicon substrates, and silicon films were deposited on gallium arsenide wafers, thereby avoiding substrate interference in the chemical analysis. Rutherford backscattering determinations of film stoichiometry were facilitated by use of hand-polished carbon substrates. Carbon is a good substrate for RBS as the energy of a backscattered alpha particle is proportional to the square of the atomic number (Z); substrates with low Z are preferred.

As previously mentioned, two alternate optical schemes (figs. II.10. and II.11.) were used in these experiments. The purpose of these two arrangements was to investigate the directionality of laser propelled particles. Substrates were positioned in both the forward and rearward hemisphere along the direction of the laser beam. The forward (S1; fig. II.11.) and rearward (S1; fig. II.10 and RS; fig. II.11.) specimens were then examined by SEM to determine the relative frequency of debris particles.

All substrates were chemically cleaned prior to insertion into the vacuum system. Trichloroethylene, acetone and methanol vapor baths were used sequentially to remove hydrocarbon impurities. Additionally gallium arsenide substrates were cleaned in vacuo by a pulsed laser method previously described in the literature.[32,33] These laser cleaning experiments were performed with a system pressure of 5×10^{-10} torr. The laser operating conditions (column II, Table II.1) and optical arrangement were such that the incident energy density was approximately 2 J/cm^2. The Auger spectrum of as-inserted gallium arsenide (fig. II.14.) showed substantial amounts of carbon (272 eV) and oxygen (510 eV) contamination prior to laser cleaning. Following 30 pulses, the Auger spectrum (fig. II.15.) showed virtually no carbon or oxygen contamination. A third spectrum (fig. II.16.) recorded immediately after 200 pulses on a mixed target ($X_{Mo,T} = 0.33$) revealed a large increase in both carbon and oxygen on the substrate.

Fig. II.14. Auger spectrum of as-inserted GaAs wafer prior to pulsed laser cleaning

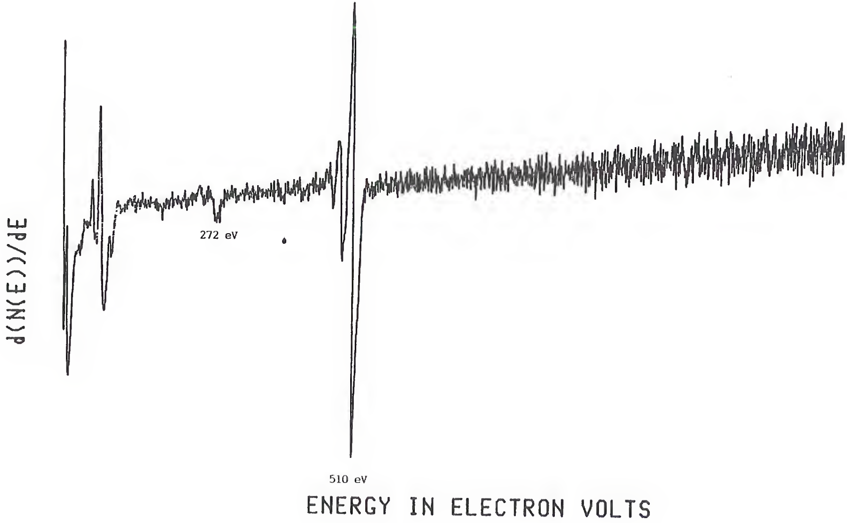
d(N(E))/dE
272 eV
510 eV
ENERGY IN ELECTRON VOLTS

Fig. II.15. Auger spectrum of GaAs wafer after thirty 2Jcm^{-2} laser pulses

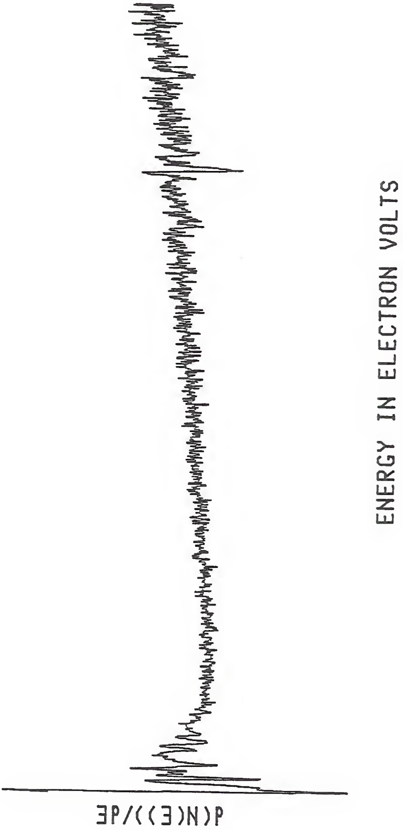
ENERGY IN ELECTRON VOLTS
d(N(E))/dE

Fig. II.16. Auger spectrum of GaAs wafer after 200 pulses on molybdenum-silicon mixture which immediately followed pulsed laser cleaning

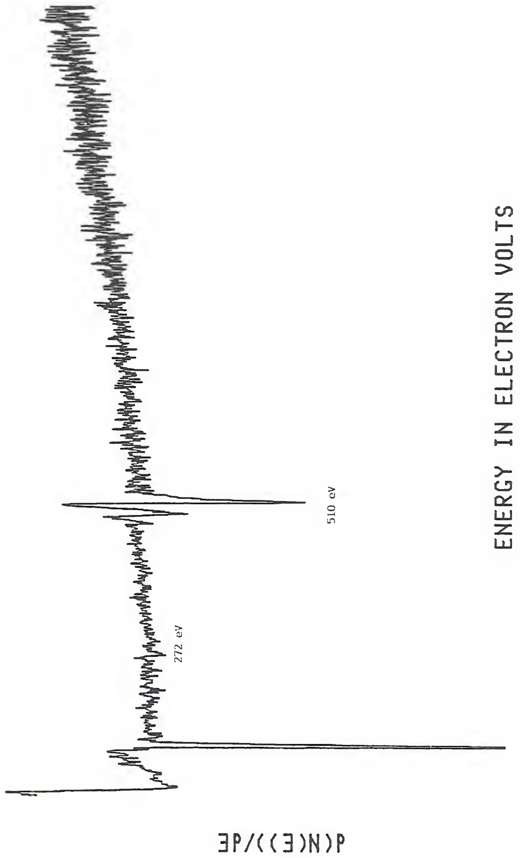
ENERGY IN ELECTRON VOLTS
510 eV
272 eV
d(N(E))/dE

AES and Scanning Electron Microscopy

Auger electron spectroscopy (AES) is an extremely useful, semi-qualitative, surface analytical technique. A monoenergetic electron beam serves to probe the uppermost 20 angstroms of a specimen. Core electrons (i.e. K shell) are ejected by the incident electron beam. The ejected core electron vacancy may then become occupied by a higher level electron (i.e. L shell). The resulting energy of this de-excitation process may subsequently be transfered to a second higher energy electron (L). If the electron resides within the uppermost 20 angstroms of specimen, it can escape without undergoing electron scattering. Electrons such as these are Auger electrons.

Auger electron spectroscopy was used extensively for both quantitative and qualitative analysis of the deposited films. First, the AES capabilities of the deposition apparatus were exploited to provide progressive in situ analysis of the substrates and developing films. Additionally, a Perkin Elmer Scanning Auger Microprobe (SAM 660) which combines the full capabilities of both AES and SEM was used to perform post-deposition analysis. The microprobe employs a single electron beam for both imaging and analysis which was selectively scanned over the surface of specimen. Non-destructive point, line and area surveys were used to determine the surface composition of the elemental and compound films. Partially destructive, compositional depth profiles of each of the films were also obtained.

SEM imaging was used to characterize film topographies, as well as to select areas for Auger analysis. The small diameter of the electron beam (<$0.5\mu m$) made it possible to examine film features selectively. For example, Auger area surveys could be performed on regions of the film containing no residual target particles. Conversely point analysis could be used to examine the composition of particles on the surface of the substrate.

Most often area surveys were performed. An area survey of each deposited film, prior to sputter ion cleaning, was recorded (fig. II.17.) over a 2300 eV energy range (30 to 2330 eV) using a 10 keV probing electron beam. Each film was subsequently cleaned by argon ion bombardment for 2 minutes using a scanning ion gun. From results obtained by similar treatment of a previously characterized molybdenum disilicide film,[29,30] it was determined that a sputtering time of 2 minutes with a scanned (raster size was selected for a 4X4 area- an uncalibrated, relative measurement of area which is specific for each instrument) ion beam was sufficient to remove adsorbed carbon and oxygen contamination. A second Auger spectrum (fig. II.18.) for each of the "clean" specimens was then recorded. Any oxygen or carbon signals in these spectra were reasoned to be incorporated film impurities arising from the deposition.

Compositional depth profiles were also recorded for most specimens (fig. II.19.). This was accomplished by alternate film removal and Auger surface analysis. Film removal rates for the argon sputter-ion gun were calibrated using a reference molybdenum disilicide film as previously described and found to

Fig. II.17. Auger spectrum of film deposited from molybdenum disilicide powder prior to sputter-ion cleaning

AES SURVEY P-C 2/27/87 AREA 1 ACQ TIME=5.50 MIN.

FILE: MoSi_8_C7 4X4 raster profile of #8

SCALE FACTOR, OFFSET=198.394, 0.000 k COUNTS/SEC BV=10.00kV BI=0.0000uA

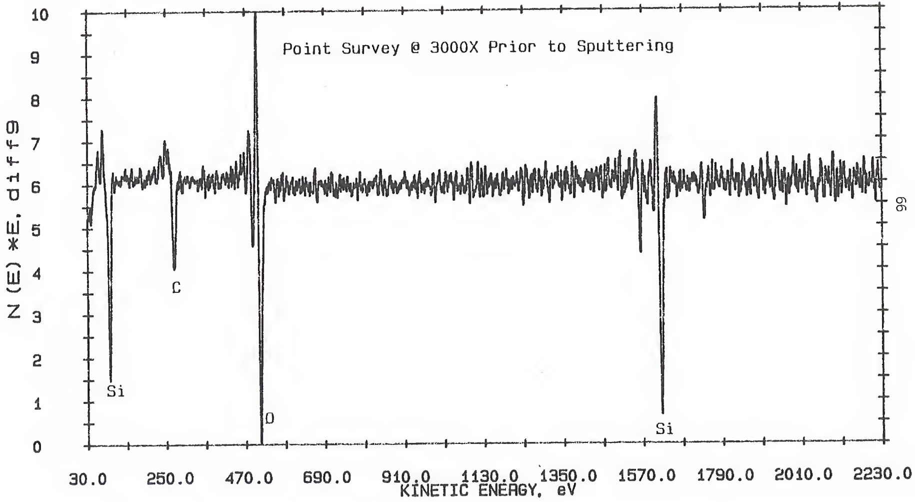

Fig. II.18. Auger spectrum of film deposited from molybdenum disilicide powder after sputter-ion cleaning

AES SURVEY P-C 2/27/87 AREA 1 ACQ TIME=5.50 MIN.

FILE: MoSi_8_C9 4X4 raster profile of #8

SCALE FACTOR, OFFSET=329.968, 0.000 k COUNTS/SEC BV=10.00kV BI=0.0000uA

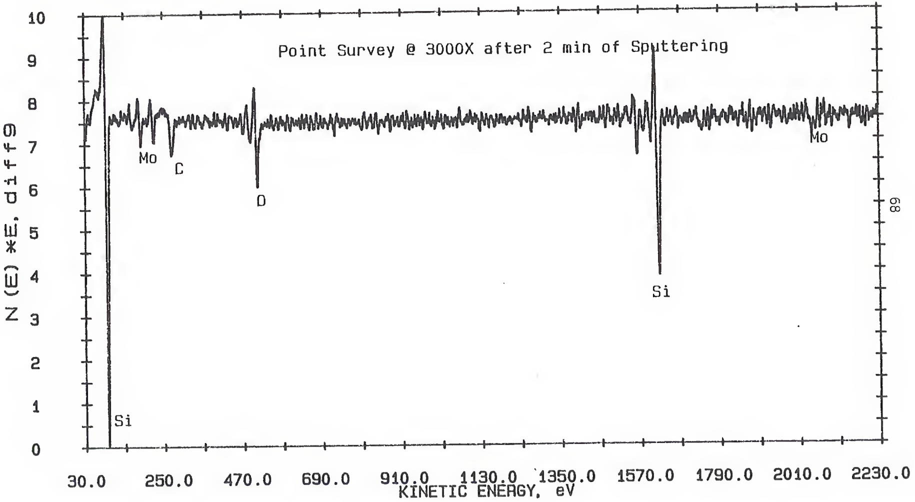

Fig. II.19. Auger compositional depth profile of molybdenum-silicide film deposited from disilicide target

AES PROFILE P-C ALT.   2/27/87   EL=Si2   REG 2 AREA 1   SPUTTER TIME=10.00 MIN.

FILE: MoSi_8_C8   4X4 raster profile of #8

SCALE FACTOR, OFFSET=190.519, 0.000 k COUNTS/SEC   BV=10.00kV BI=0.0000uA

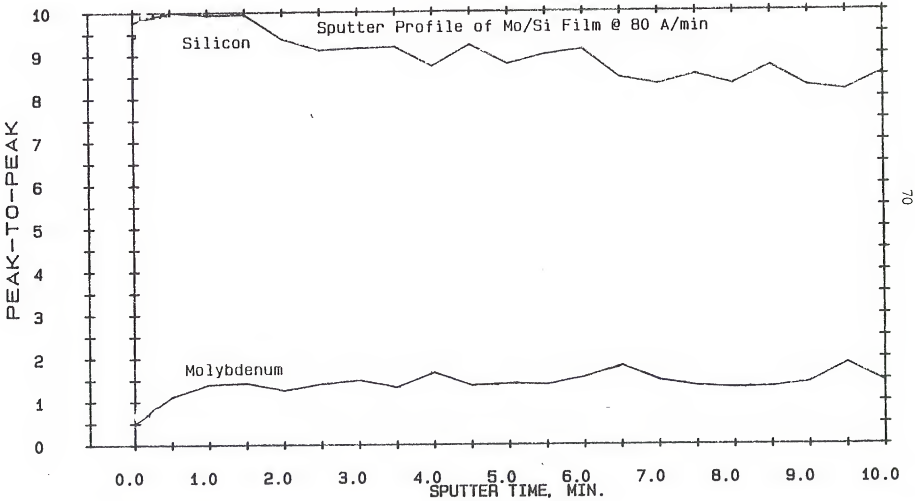

be 80 Å per minute for 4X4 raster area. The surface composition was then displayed versus sputtering time. This process provided data used for quantitative analysis of film stoichiometry and thickness.

In some cases line scans of the electron beam across the sample were used to investigate the compositional variance of the surface. The numbers of Auger electrons of a given energy measured by selecting energy "windows," which correspond to the most intense Auger transition of an element of interest, were recorded as a function of beam travel. The response within a given energy window was digitally converted to atomic percent of the corresponding element and displayed as atomic concentration versus distance (fig. II.20.). These line profiles were then correlated with SEM photographs to study differences in composition between residual target particles and the deposited films.

Alternatively, point analyses (fig. II.21.) of residual particles following by repeated intermittent argon-ion bombardment were used to investigate the compositional changes of the targets due to laser heating.

Rutherford Backscattering Spectroscopy

Rutherford backscattering spectroscopy (RBS), the detection of alpha particles scattered through large angles (the classical Rutherford experiment), was also used for non-destructive. compositional depth profiling of each of the deposited molybdenum

Fig. II.20. Auger compositional profile as a function of beam travel across specimen

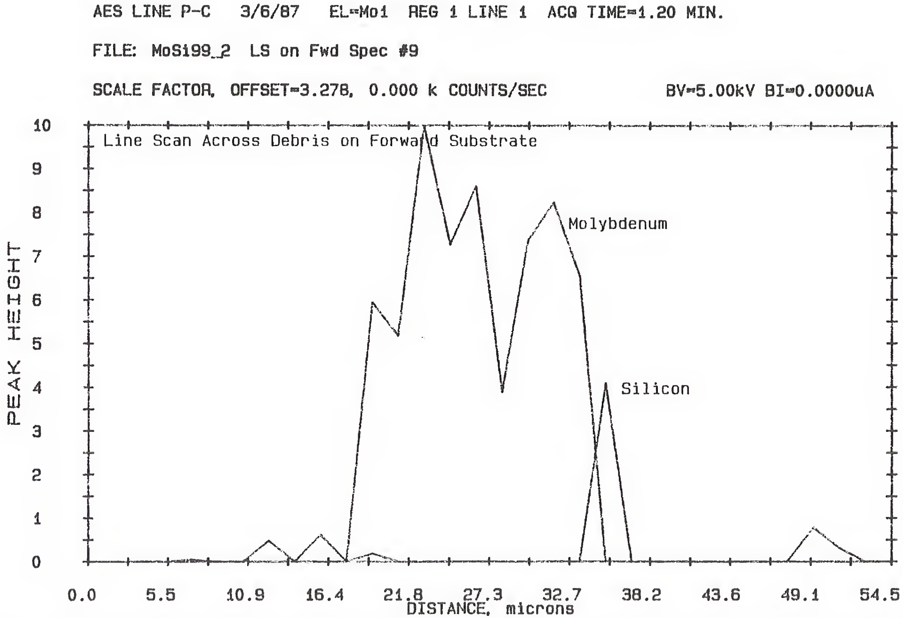
AES LINE P-C 3/6/87 EL=Mo1 REG 1 LINE 1 ACQ TIME=1.20 MIN.
FILE: MoSi99_2 LS on Fwd Spec #9
SCALE FACTOR, OFFSET=3.278, 0.000 k COUNTS/SEC BV=5.00kV BI=0.0000uA
Line Scan Across Debris on Forward Substrate
Molybdenum
Silicon
PEAK HEIGHT
0
1
2
3
4
5
6
7
8
9
10
0.0
5.5
10.9
16.4
21.8
27.3
32.7
38.2
43.6
49.1
54.5
DISTANCE, microns

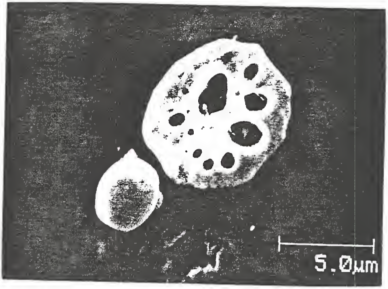

Fig. II.21. SEM photograph of two molybdenum disilicide residual particles. The numbers indicate points for AES Analysis

silicide films. Quantitative stoichiometric analysis was performed without the use of compositional standards. The composition of the molybdenum disilicide film used for reference in AES and ESCA studies was also varified using RBS.

The silicide samples were irradiated by a monoenergetic (2 MeV) alpha particle beam generated by a Van de Graaff generator.[34] The range of beam currrents used was from 20 to 200 nA, and the analysis area was approximately 1.5 mm^2. Large angle scattering events (170 degrees) were detected by a surface barrier detector subtending a solid angle of 4×10^{-4} sr. The resulting voltage pulses were then sorted and stored by a multichannel analyzer in the pulse height analysis mode.[34] The number of scattering events was then displayed versus backscattered alpha energy (fig. II.22.).

Electron Spectroscopy for Chemical Analysis

A Perkin Elmer model 5100 X-ray photoelectron spectrometer was used to record MgKα XPS or (as otherwise known) ESCA spectra for each of the silicide films. An ESCA survey (fig. II.23.) for each specimen over a range of binding energies from 1100 to 0 eV was recorded prior to suface cleaning by argon ion bombardment. Subsequently the specimens were sputtered to remove surface adsorbed carbon and oxygen, and a second survey (fig. II.24.) was recorded. Thus the degree and nature of film contamination was examined by ESCA analysis also. Additionally the binding

Fig. II.22. Rutherford backscattering spectrum. The ordinate has units of counts. The abscissa has units of energy

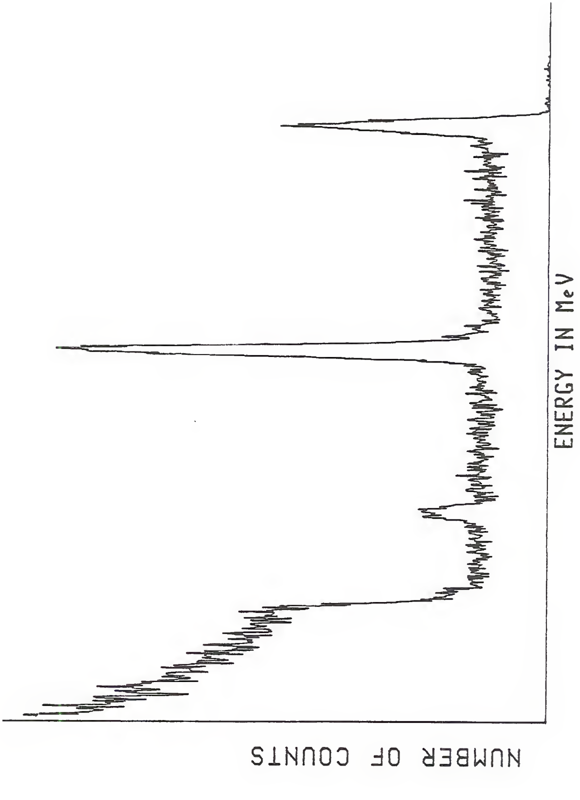
ENERGY IN MeV
NUMBER OF COUNTS

Fig. II.23. ESCA survey spectrum of molybdenum disilicide film prior to sputter-ion cleaning

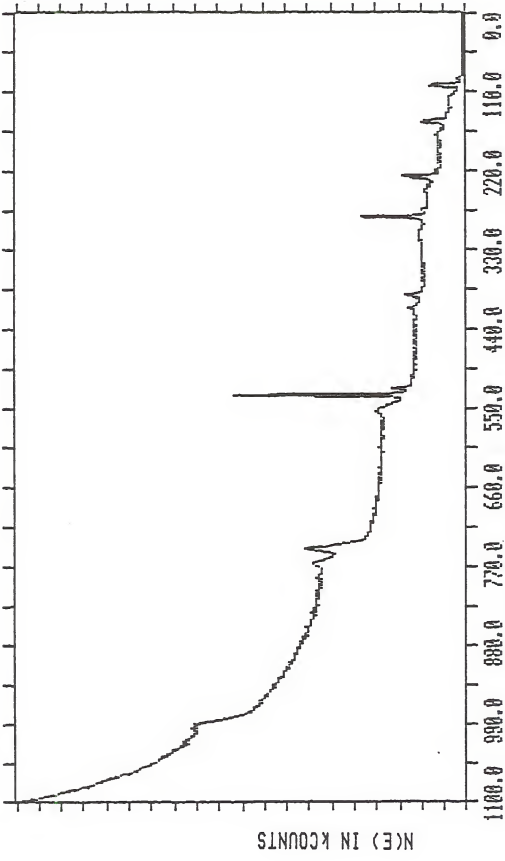
N(E) IN KCOUNTS
BINDING ENERGY IN eV
1100.0
990.0
880.0
770.0
660.0
550.0
440.0
330.0
220.0
110.0
0.0

Fig. II.24. ESCA survey spectrum of molybdenum disilicide film following sputter-ion cleaning

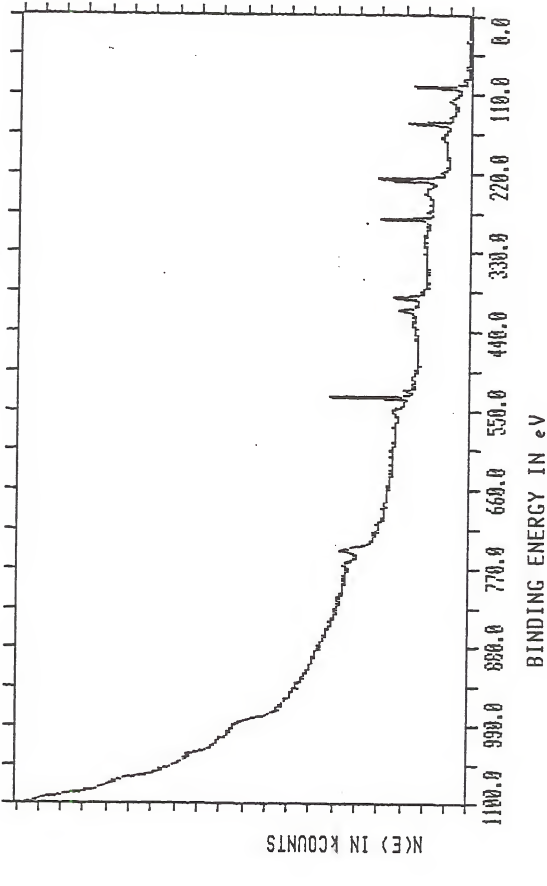
N(E) IN KCOUNTS
BINDING ENERGY IN eV
1100.0
990.0
880.0
770.0
660.0
550.0
440.0
330.0
220.0
110.0
0.0

energies, chemical shifts and peak areas were recorded for each of the peaks of interest occurring in the parent survey. This was accomplished by a method of multiplexing (a phenomenological definition of multiplexing is the examination of a large number of selected energy windows containing the peaks of interest). Typical multiplex spectra obtained from a molybdenum silicide film include the following binding energy windows: 420 to 390 eV (containing the $3p_{1/2}$ and $3p_{3/2}$ transitions for molybdenum; fig. II.25.); 243 to 223 eV (containing the $3d_{3/2}$ and $3d_{5/2}$ transitions for molybdenum; fig. II.26.); 165 to 145 eV (containing the silcon 2s transition; fig. II.27.); and 115 to 95 eV (containing the silicon 2p transition; fig. II.28.).

Methods of Quantitative Analysis

Each of the surface analytical instruments was used to perform quantitative analysis of the molybdenum-silicon stoichiometry of the films. Only for RBS was it possible to deduce film composition without the aid of a molybdenum silicide standard. The film thicknesses were measured, exclusively, by the destructive AES depth profiling technique previously described.

RBS determination of film stoichiometry. A method described by Foti et al.[35] was used to determine the relative concentrations of molybdenum and silicon in the films from RBS

Fig. II.25. ESCA multiplex spectrum of molybdenum $3p_{1/2}$ and $3p_{3/2}$ transitions. (410 eV and 393 eV respectively)

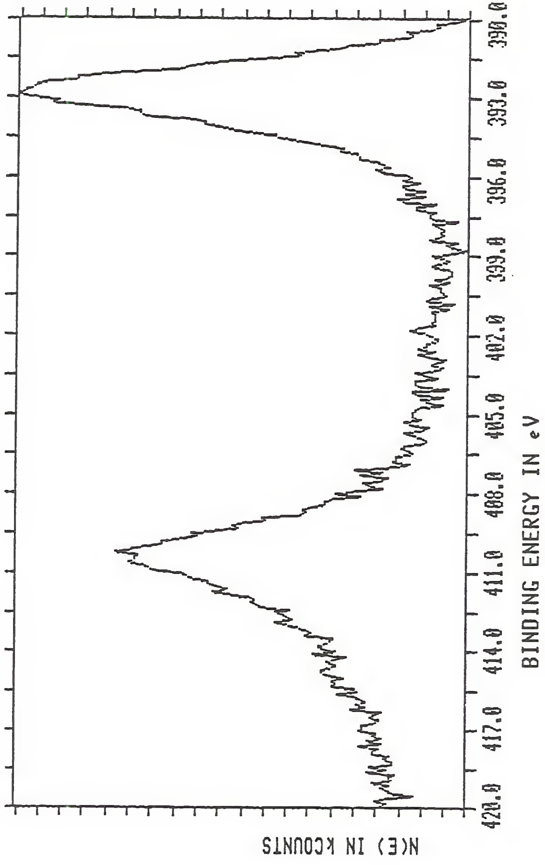
N(E) IN KCOUNTS
BINDING ENERGY IN eV
390.0
393.0
396.0
399.0
402.0
405.0
408.0
411.0
414.0
417.0
420.0

Fig. II.26. ESCA multiplex spectrum of molybdenum $3d_{3/2}$ and $3d_{5/2}$ transitions. (230 eV and 227 eV respectively)

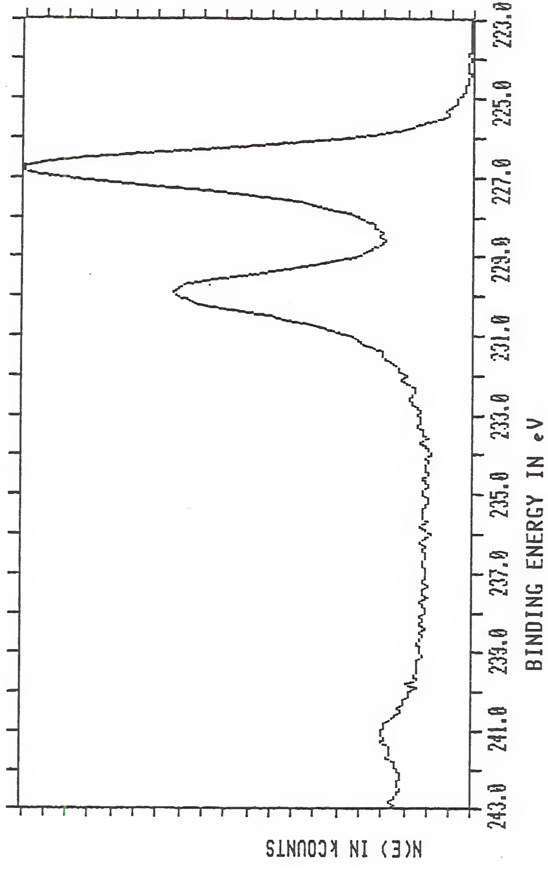
223.0
225.0
227.0
229.0
231.0
233.0
235.0
237.0
239.0
241.0
243.0
BINDING ENERGY IN eV
N(E) IN KCOUNTS

Fig. II.27. ESCA multiplex spectrum of silicon 2s transition (150 eV)

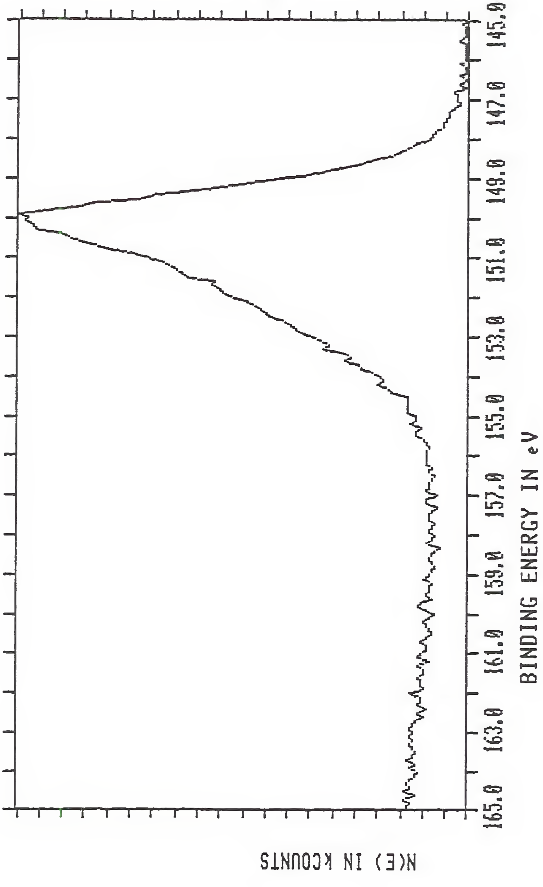
145.0
147.0
149.0
151.0
153.0
155.0
157.0
159.0
161.0
163.0
165.0
BINDING ENERGY IN eV
N(E) IN KCOUNTS

Fig. II.28. ESCA multiplex spectrum of silicon 2p transition (98.5 eV)

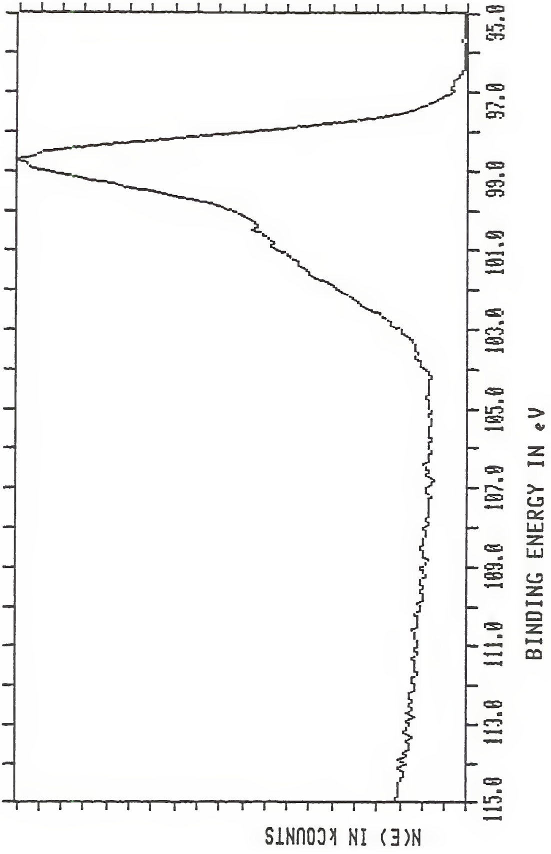
95.0
97.0
99.0
101.0
103.0
105.0
107.0
109.0
111.0
113.0
115.0
BINDING ENERGY IN eV
N(E) IN KCOUNTS

peak areas. Accordingly the ratio of the number of silicon atoms (N_{Si}) to the number of molybdenum atoms (N_{Mo}) in the films was obtained using the following expression:

$$\frac{N_{Si}}{N_{Mo}} = \frac{\sigma_{Mo} \cdot A_{Si}}{\sigma_{Si} \cdot A_{Mo}} \qquad \text{II.7.}$$

where the A_i are the peak areas determined for silicon and molybdenum and expressed as a number of counts and σ_{Mo} and σ_{Si} are the differential scattering cross sections for the molybdenum and silicon respectively. The differential scattering cross section may be computed as follows:

$$\sigma_i = \left[\frac{Z_i Z_\alpha e^2}{4E}\right]^2 \frac{4}{\sin^4\Theta} \frac{\{\cos\Theta + \sqrt{1 - [(M_\alpha/M_i)\cdot\sin\Theta]^2}\}^2}{\sqrt{1 \ [(M_\alpha/M_i)\cdot\sin\Theta]^2}}$$

II.8.

Here Z_α is the atomic number for the alpha particle (2 for He); Z_i is the atomic number for the scattering element of interest (14 for Si; 42 for Mo); E (2 MeV) is the energy of the incident alpha particles; M_α is the mass of an alpha particle; M_i is the mass of the scattering atom and Θ (170°) is the angle between the detector normal and the incident beam (sample surface normal): Z, E, M_α and Θ were constant and independent of the scattering element. The values for the total scattering cross sections were obtained from tabulations compiled by Foti et al.[35] At large angles the ratio σ_{Mo}/σ_{Si} reduces to

$$\frac{\sigma_{Mo}}{\sigma_{Si}} = \frac{Z^2_{Mo}}{Z^2_{Si}} \qquad \text{II.9}$$

Using values obtained either from the tabulated total scattering cross sections or from equation II.9) equation II.7 may be rewritten to express the mole fraction of molybdenum in the films as a function of peak areas only:

$$X_{Mo} = [9\cdot(A_{Si}/A_{Mo})-1]^{-1} \qquad \text{II.10}$$

The peak areas for molybdenum and silicon were obtained using data stored by the multichannel analyzer. The number of counts contributing to the peak of each element were obtained by two different methods.

Identification of the maximum energy for molybdenum scattered alphas was difficult as in most cases there was not a level baseline at high energy (fig. II.22.). A digital method for correcting peak areas for inclusion of baseline counts was used. The resulting net area (A_{net}) was used for the area of the molybdenum in all cases.

Conversely a level, uniform baseline on either side of the silicon peak facilitated its peak area measurement. Thus the peak area for silicon was obtained from the gross number of counts in the silicon region of each spectrum. (A_{gross}). Hence the molybdenum concentration for each film was computed as follows:

$$X_{Mo} = [9\cdot(A_{Si,gross}/A_{Mo,net})-1]^{-1} \qquad \text{II.11.}$$

It should be noted that any systematic error introduced by this treatment of peak areas would result in higher values for X_{Mo}

Film stoichiometry from AES. The relative atomic concentrations of silicon and molybdenum were also determined using data obtained from AES compositional depth profiling (fig. II.20.). A first order approximation to quantitative analysis in Auger spectroscopy, as reported by Palmberg et al.[36], was used as a guide for these determinations. In this approximation the atomic concentration of an element in a compound film was obtained from relative intensity measurements of the elements in both the compound sample and elemental standards:

$$C_x = I_x/I_{x,std} \qquad \text{II.12.}$$

where I_x and $I_{x,std}$ are the Auger currents from the sample and elemental standard respectively. Instead of elemental standards the molybdenum disilicide film previously descibed was used to evaluate relative sensitivities of molybdenum and silicon in the compound films. The relative sensitivity (ς_s) was computed, using measured Auger peak heights, as follows:

$$\varsigma_s = S_{Si}/S_{Mo} = I_{Si,MoSi_2}/2I_{Mo,MoSi_2} \qquad \text{II.13.}$$

where S_i is the elemental sensitivity; and, $I_{i,MoSi_2}$ is the Auger intensity for the element molybdenum disilicide standard. The factor 2 arose from the known ratio of silicon to molybdenum (2:1) in the film. The ratio of sensitivities was measured and found to be 1.6.

The atomic ratio of silicon to molybdenum was then computed using

$$N_{Si}/N_{Mo} = \varsigma_s \cdot I_{Si}/I_{Mo} \qquad \text{II.14.}$$

where I_i was the peak height of the ith element determined from differentiated Auger spectra for each of the films determinied.

The mole fractions of molybdenum in the films were calculated as follows:

$$X_{Mo} = [(\varsigma_s \cdot I_{Si}/I_{Mo})-1]^{-1} \qquad \text{II.15.}$$

and found to be in reasonable agreement with those computed from RBS data.

Film stoichiometry from ESCA. Additionally multiplex data from ESCA analysis were reduced to obtain quantitative film stoichiometry for each of the compound films. Again, a molybdenum disilicide standard was used. The peak areas corresponding to silicon and molybdenum transitions were integrated for each of the sample films and for the standard. The sample peak areas were normalized using the corresponding peak area information obtained from the standard film. The atomic ratios for each of the six possible permutations (3 molybdenum transitions and 2 silicon transitions) were averaged to obtain an estimate of the mole fraction of molybdenum contained in each of the films. With only one exception (Sample # 5; Table IV.4.) these estimates were in close agreement with both RBS and AES values.

Film thickness determinations. Film thicknesses were obtained exclusively from AES compositional depth profiles. AES depth profiles (e.g fig. 20) of each of the films, including analysis for Mo, Si, C and O, were used to estimate the time required for sputtering through the deposited films (τ_s). A noteable increase in the C signal (the substrate was typically carbon) or a significant decrease in both the silicon and molybdenum signal was used as a determinators for this estimation. The sputtering rate for a 4 X 4 raster of the Perkin Elmer SAM 660 argon sputter-ion gun was calibrated in a similar fashion using a 1000 Å molybdenum disilicide film (fig. II.29.). For that instrument a rate of 80 Å/min for molybdenum disilicide was found (this was in reasonable agreement with the rate found for tantalum oxide- a frequently used standard for sputter rate determinations- of 100 Å/min).

The film thickness for each of the deposited films was determined using the sputtering time and rate as follows:

$$h_f = \tau_s \cdot \xi_s \qquad \text{II.16.}$$

where h_f is the film thickness and ξ_s (80 Å/min) is the sputtering rate.

Fig. II.29. Auger compositional depth profile of molybdenum disilicide film used as reference

AES PROFILE V/F ALT. 3/2/87 EL=Mo1 REG 2 AREA 1 SPUTTER TIME=16.00 MIN.

FILE: DiSi_2 Kelly's 1000 A Moly Disilicide for Reference Data

SCALE FACTOR, OFFSET=92.423, 0.000 k COUNTS/SEC BV=10.00kV BI=0.0000uA

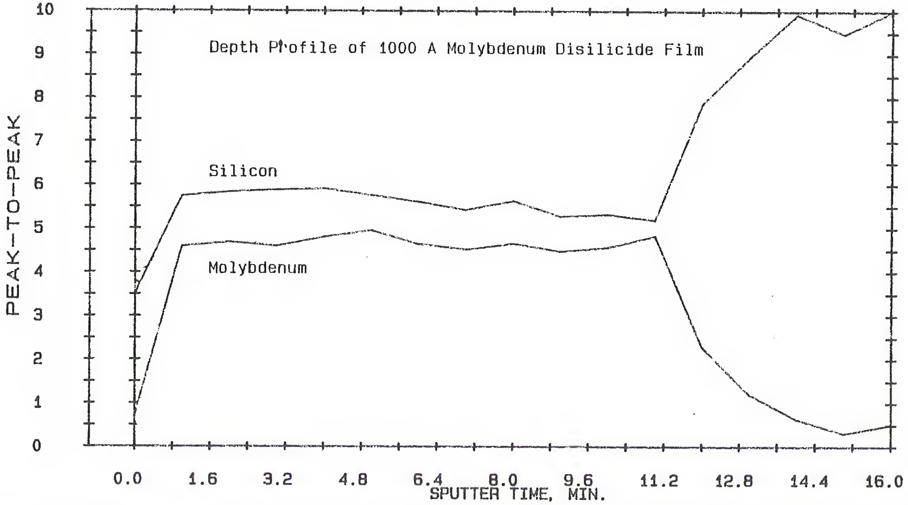

CHAPTER III
THEORY

The kinetics of heating play a significant role in the mechanism of evaporation. For conventional sources the temperature of the material will normally rise only as high as the boiling temperature. Additionally, the entire bulk of material must rise to the boiling temperature.

Laser heating with lasers having short pulse durations is highly surface selective. The light energy is deposited in the material and converted to thermal energy so rapidly that bulk diffusion of heat is insignificant.[17,18,21]

For solids the absorption coefficient is dependent on the band structure and hence varies with wavelength. At the melting point, however, metals and metalloids such as silicon have similar absorption coefficients at all wavelengths- on the order of 10^6 cm^{-1}. The corresponding absorption depth for most metals is of the order of 100 Å.

Prevalent theories of laser heating[14-19] consider two general regimes of laser ablation: (1) for power densities below $10^6 W/cm^2$ and pulse durations <1 msec where vaporization is described adequately by the conventional description of boiling[17]; and (2) for power densities greater than $10^6 W/cm^2$ and short pulse durations (< 1 msec) where vaporization is explosive.

Krokhin[18] and others[14-17,19] have derived relationships which enable explicit calculations of the temperature rise for laser-irradiated solids. In this chapter the methods of Krokhin[18] as well as the Hertz-Knudsen-Langmuir equation are used to calculate hypothetical evaporation for laser-heated solids in vacuo. Additionally, the effect of the target particle size on the composition of films deposited from powder mixtures is described.

Conventional Evaporation

The saturated vapor pressure, heat of vaporization and boiling temperature are equilibrium thermophysical properties. These quantities are nonetheless useful for predicting the limits for non equilibrium physical behavior (i.e. evaporation). For example, the Hertz-Knudsen-Langmuir (HKL) equation for the mass evaporation rate expresses mass efflux from an evaporating surface as a linear function of the equilibrium vapor pressure (p_s):

$$\Gamma_m = (\partial m/A_s \partial t) = \alpha_v\{M/(2\pi RT)\}^{1/2}(p_s - p) \qquad \text{(III.1.)}$$

where Γ_m is the mass flux , M is the gram molecular weight; R is the ideal gas constant; A_s is the total surface area; t is time; T is the temperature of the vapor; α_v is a dimensionless ideality factor known as the vaporization coefficient and p is the hydrostatic pressure. The Hertz-Knudsen-Langmuir equation is but one of many relationships which have been derived from a generally accepted model for bulk vaporization. This model, outlined by Baker et. al.[24] and illustrated in fig. III.1. considers evaporation as the net transfer of mass across a finite, non-equilibrium phase interface (known as the Knudsen layer) which extends outward from the solid interface a distance of a few mean free paths. The difference in pressure across the Knudsen layer (p_s-p) expressed in equation III.1. relates the measureable macroscopic pressure (p) to the vapor pressure in the vicinity of the solid. More general non-linear analytical methods include variations in temperature as well. Approximate evaporation rates may be calculated using the HKL equation. The assumption that temperature is everywhere the same (implicit in equation III.1.) results in a tremendous simplification of the evaporation rate formalism. Further simplifications may be made for the hypothetical case of ideal (α_v= 1) vaporization in a vacuum (p = 0).

$$\Gamma_m = \sqrt{\{M/(2\pi RT)\}} \cdot p_s \qquad \text{III.2.}$$

These simplifications expectedly lead to inaccuracies in absolute evaporation rate calculations, especially due to the neglect of temperature variation across the Knudsen layer.[24] However, when rewritten for two condensed species raised to the temperature at which their vapor pressures are equal to the ambient pressure. as in equation III.3.

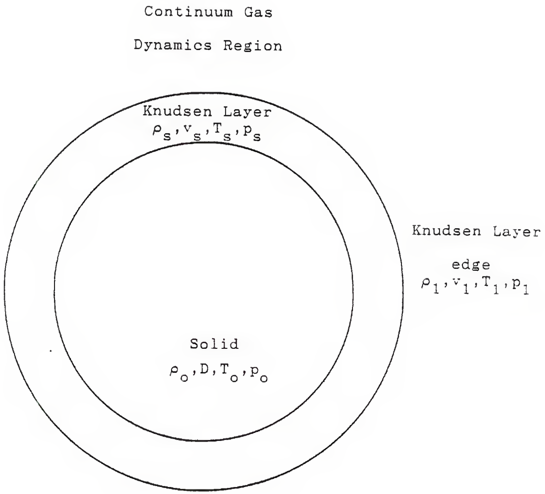

Fig. III.1. Knudsen layer model of evaporation

$$\Gamma_{m,x}/\Gamma_{m,y} = \left[\frac{M_xT_y}{M_yT_x}\right]^{1/2} \qquad \text{III.3.a.}$$

reasonable estimates for the relative volatilities of mixture constituents are obtained. Equation III.3. constitutes an "equilibrium" model for the co-evaporation of two elements. The temperatures (T_i) are obtained from compiled temperature dependent vapor pressure data[37] using the ambient pressure in the deposition vessel for p_s and the Clapeyron equation (Appendix B). In the previously described experiments, mixtures of molybdenum and silicon powders were heated in a vacuum by intense laser radiation. The resulting film composition is governed not only by the ratio of volatilities but also by the ratio of exposed surface areas of the mixture constituents. From equations III.1. and III.3.a. an expression for the mole fraction of a single constituent (X_y) in the films may be obtained:

$$X_y = \left[(A_x/A_y)\cdot\left[M_xT_y/M_yT_x\right]^{1/2} + 1\right]^{-1} \qquad \text{III.3.b.}$$

The ratio of surface areas for constituent target particles (A_x/A_y) is obtained from either specific surface area or size distribution measurements.

Laser Evaporation

The process of laser evaporation is one that has been reviewed by many.[10,13-22] Laser vaporization may be considered to occur in three steps: 1) absorption of photons by the irradiated material, 2) photon-phonon energy transfer (degradation to heat) and 3) supply of latent heat of vaporization to the surface. The mechanisms of photon absorption and energy transfer as well as the heated depths differ for metals and semiconductors.[21] In metals photons are absorbed by the large density of conduction electrons via an internal photoeffect. The electrons are raised to higher energy states within the conduction band (intraband)[17,21] For low intensity laser illumination of elemental semiconductors such as silicon or germanium, absorption by direct interband transitions (the typical absorption mechanism for compound semiconductors) is forbidden. Absorbtion occurs indirectly by emission or absorption of phonons. At high intensities ($J > 10^6$ W/cm^2), however, free carrier densities in excess of 10^{19}/cm^3 are created in times less than the pulse duration resulting in the creation of a free carrier plasma and an enhanced absorption coefficient.[21] Heat generation in metals occurs via electron-phonon collisions. In a good conductor the mean free time between collisions is of the order of 10^{-12} to 10^{-13} seconds. During the time of a typical laser pulse (τ_p for Lumonics TEA CO_2 laser is 2.5×10^{-7} seconds) the electrons will undergo many collisions with the lattice. Thus the photon energy is essentially instantaneously converted into heat within the volume in which the light is absorbed.[17] Heat generation within semiconductors occurs via carrier-phonon interactions. For free carrier concentrations below a critical value ($2 \times 10^{21} \mathrm{cm}^3$ in silicon) the mean free time between collisions is on the order of 10^{-11} seconds, and most of the absorbed energy is given up to the lattice. Above this characteristic threshold a significant portion of the absorbed energy gives rise to Auger recombinations resulting in a reduction of the temperature rise and less efficient coupling.[21]

The kinetics of vaporization and the depths to which the irradiated material is heated depend largely on the pulse duration. A qualitative description of the effect of pulse shape on laser heating of metals is given by Ready:[17] "A shorter, higher power density pulse leads to considerably higher peak surface temperature than a longer, lower power density pulse of the same total energy, which produces a more uniform temperature distribution and a greater depth of penetration." (p. 465) In the case of silicon the absorption length is small for infrared radiation, and light energy is deposited in the vicinity of the surface. The energy density required to bring the surface to a given temperature is proportional to the square root of the pulse duration and is independent of the absorption coefficient.[21]

Krokhin[18] further differentiates the process of laser heating into two temperture (and consequently power density) regimes. At power densities above the minimum threshold for vaporization 10^6W/cm^2 and below 10^8 W/cm^2 the evaporated material is a transparent gas. At power densities greater than 10^9 W/cm^2 surface temperatures are attained where significant ionization and atomic excitation begins. The evaporated substance is converted into a plasma state where it is largely or fully ionized.

Low Temperature Laser Evaporation

In the low temperature regime the dynamics of evaporation are governed by the conditions of the evaporation front[18] (the Knudsen layer edge).[21] The mass evaporation rate equation is accordingly obtained from gas dynamic relationships. The continuity equation (III.4.a.), the Euler equation (III.4.b.) and the equation for the conservation of energy for adiabatic expansion of the vapor (III.4.c.):

$$\frac{\partial \rho}{\partial t} + \nabla \cdot (\rho v) = 0 \qquad \text{III.4.a.}$$

$$\frac{\partial v}{\partial t} + (v \cdot \nabla)v + \frac{1}{\rho}\nabla \cdot p = 0 \qquad \text{III.4.b.}$$

$$\frac{\partial}{\partial t}\left(\rho\epsilon + \frac{1}{2}\rho v^2\right) + \nabla \cdot \left[\rho v\left(\epsilon + \frac{1}{2}v^2 + \frac{p}{\rho}\right)\right] = 0 \qquad \text{III.4.c.}$$

are solved by a method prescribed by Krokhin[18] where ρ is the gas density, t is time, v is the velocity of the gas, p is pressure and ϵ is the specific internal energy.

An appropriate equation of state is written as:

$$\epsilon = \left(\frac{p}{\gamma - 1}\right)\rho + U \qquad \text{III.5.}$$

where γ is the heat capacity ratio for the gas and U is the specific sublimation energy. Additional boundary conditions which account for the discontinuities at the surface (fig. III.1; Knudsen layer model) are invoked and are written in equations III.6.a.-III.6.c.

The equation for conservation of mass is written as follows:

$$\rho_o D = \rho_1 (v_1 - D) \qquad \text{III.6.a.}$$

where ρ_o is the density of the solid, v_1 is the velocity of the vapor and D is the inward velocity of the vaporization wave.

Conservation of momentum is written to account for the pressure on the condensed surface due to evaporation:

$$p_o = p_1 + \rho_o D v_1 \qquad \text{III.6.b.}$$

where p_o is the recoil pressure created (as in rocket propulsion) by the momentum carried with the evaporated atoms.

Finally, a power balance equation is written as follows:

$$q_1 = \rho_o D(\epsilon_1 + \frac{1}{2} v_1^2) + p_1 v_1 \qquad \text{III.6.c.}$$

where q_1 is the absorbed part of the laser power density.

Two further equations relate the gas dynamic variables: p_1, ρ_1, v_1 and ϵ_1 to those of the solid: D and ρ_o. The first relation is the Jouguet condition for quasi-stationary evaporation:

$$D = v_1 - c_1 = v_1 - \sqrt{\gamma(p_1/\rho_1)} \qquad \text{III.7.}$$

which states that the relative velocity of the vapor and solid should not exceed the sound velocity (c_1) near the surface of the solid. The second relation describes the evaporation process at the surface:

$$p_s = p_1 + \rho_o D v_1 \qquad \text{III.8.}$$

where p_s is the saturated vapor pressure.

A parametric solution to the resulting system of differential equations containing equations III.4.a.-III.4.c. and these boundary conditions is obtained by selecting appropriate self-similar variables for pressure, velocity and density:

$$\lambda_1 = - \left[1 + \frac{(\gamma-1)^2 \lambda_2^2}{2(\gamma+1)} \right]^{-1} \qquad \text{III.9.}$$

and

$$\lambda_2 = \frac{\dfrac{\gamma(\gamma+1)^2}{(\gamma-1)^2}}{\ln\left[\left[\dfrac{(\gamma-1)^2 \ \lambda_2^3}{2(\gamma+1)} \right] + \dfrac{(\gamma-1)\cdot\lambda_2}{(\gamma+1)^2} \right] - \ln\left[\dfrac{q_o A}{U^{3/2}} \right]} \qquad \text{III.10.}$$

Here λ_1 and λ_2 are constant velocity parameters related respectively to the propagation velocity of the ablation wave in the solid and the Knudsen layer edge velocity. The incident power density q_o is taken to be equal to the absorbed power density (i.e. reflective losses are ignored in this case) and A is the preexponential factor for the integrated Clausius equation assuming the ideal gas equation of state (Appendix C)

Equations III.9. and III.10 may be solved iteratively (Appendix D) to give approximate expressions for the vapor density, the vapor velocity, the pressure of the vapor, the temperature of the vapor and the velocity of the evaporation front. The product of the latter quantity with the true density of the solid yields the mass evaporation flux:

$$\rho_o D = \Gamma_m \qquad \text{III.11.}$$

which is the principal quantity of interest for thin-film applications. The mass evaporation rates for silicon and three refractory metals are calculated for three laser power densities. (Appendix E).

High Temperature Laser Evaporation

At high power densities ($\geq 10^9$ W/cm^2) the temperature of the effluent vapor is high enough to cause appreciable atomic excitation and ionization.[18,19] At this point the vapor is no longer transparent to subsequent radiation. The vapor absorbs further energy via an inverse Bremsstrahlung process and is thus no longer expanded adiabatically. Krokhin[18] derives approximate analytic expressions for the specific internal energy, temperature and mass of a plasma as a function of its absorption coefficient (k), the focal radius of the laser (r_o) and the absorbed laser power density (Q) by assuming a self-matched regime. The self-matched regime is one in which the optical thickness remains constant.

The plasma absorption coefficient for light $\frac{hc}{2\pi\lambda} \ll kT$ is determined primarily by the inverse Bremsstrahlung contribution[18-20] and is given by

$$k = 0.070 \frac{Z(Z+1)^2}{\omega^2 T^{3/2}} N_o^2 \qquad \text{III.12.}$$

where Z is the average ionic charge, N_o is the atomic density of the solid and ω is the frequency of the laser radiation. The results of Krokin[18] are

$$\epsilon = [(2\pi)^{\alpha} k_o^{-1} r_o^{2\alpha-1} (Qr_o^2/d^2)^{-\alpha}]^{2/(2\beta-3\alpha)} \qquad \text{III.13.}$$

$$\rho = (Q/2\pi d^2)\ [(2\pi)^{\alpha} k_o^{-1} r_o^{2\alpha-1} (Qr_o^2/d^2)^{-\alpha}]^{-3/(2\beta-3\alpha)} \qquad \text{III.14.}$$

$$M = \pi r_o^2 t\ [(2\pi)^{\alpha} k_o^{-1} r_o^{2\alpha-1} (Qr_o^2/d^2)^{-\alpha}]^{2/(2\beta-3\alpha)} \qquad \text{III.15.}$$

for specific internal energy, density, and mass of the plasma, respectively. For a fully ionized gas the exponents are $\alpha = 2$; $\beta = -3/2$ and k_o is $2.18 \times 10^{29}\ Z^3(Z+1)^{3/2} G_{AW}$ and d is the radius of the particle.

The relative concentration of mixture constituents is thus obtained as follows:

$$N_x/N_y = \frac{M_x G_y}{M_y G_x} \qquad \text{III.16.}$$

Where G_i is the gram atomic weight of the ith species.

Influence of Particle Size on Film Composition and Deposition Rate

The evaporation rate is proportional to the area of the evaporating surface:

$$\Gamma = \Gamma_m A_s \qquad \text{III.17.}$$

where Γ is the evaporation rate, Γ_m is the mass flux of evaporant atoms and A_s is the total surface area evaporating. Clearly the total surface area for each constituent in an evaporating mixture influences the resulting composition of the film (fig. III.2.) Whereas the total surface area of a sample of spherical particles is directly proportional to the square of the particle radius, the specific surface area $[l^2,m^{-1}]$ varies inversely with the radius. The expected film stoichiometry is thus be predicted from calculated evaporation rates and measured specific surface areas. In general, the predicted mole fraction for a single consituent in a binary compound film which is formed from evaporating mixtures of free-falling powders is

$$X_y = \left[\frac{w_x \cdot S_x \cdot \bar{\Gamma}_x}{w_y \cdot S_y \cdot \bar{\Gamma}_y} + 1 \right]^{-1} \qquad \text{III.18.}$$

where w_i is the weight of the ith constituent, S_i is its specific surface area and $\bar{\Gamma}_i$ is the molar evaporation flux of the ith

Fig. III.2. Graph of mole fraction molybdenum in film vs mole fraction of molybdenum in a target mixture with specific surface ratio as a parameter

I $A_{Mo}/A_{Si} = .1$
II $A_{Mo}/A_{Si} = 1$
III $A_{Mo}/A_{Si} = 10$

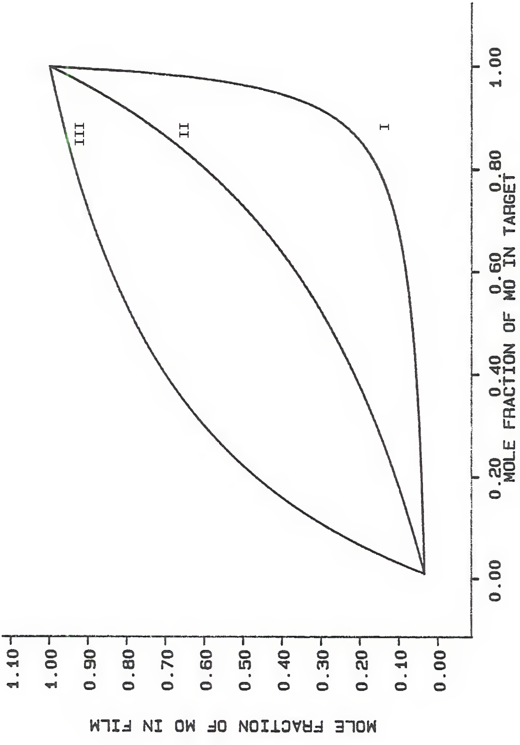
MOLE FRACTION OF MO IN FILM
0.00
0.10
0.20
0.30
0.40
0.50
0.60
0.70
0.80
0.90
1.00
1.10
MOLE FRACTION OF MO IN TARGET
0.00
0.20
0.40
0.60
0.80
1.00
I
II
III

constituent. The expected mole fractions of molybdenum for each molybdenum-silicon mixture are calculated thusly for each of the foregoing models of evaporation and for several laser power densities.

CHAPTER IV
RESULTS AND DISCUSSION

The advantages of direct laser evaporation of solids over conventional vacuum thin-film deposition techniques are reviewed in Chapter I. Two principal difficulties associated with the existing technology hinder its acceptance and widespread use: 1) Typically, the intense laser-solid interaction produces large amounts of "splatter" which is incorporated into the resulting films rendering them useless for most optical and microelectronic applications; and 2) Stoichiometric deposition of compounds composed of elements having widely different enthalpies of vaporization is generally not possible.[1,2]

In this chapter the theoretical and experimental results are given for laser evaporation of targets having compositions within the molybdenum-silicon binary alloy system. The molybdenum-silicon system is of interest for its potential technological importance in the microelectronics industry. More significantly, molybdenum and silicon have relatively large differences in volatilities while each has a low vapor pressure at elevated temperatures. Thus a successful application of this new technique to the molybdenum-silicon system demonstrates a general utility for compound thin-film deposition.

The results of these experiments are classified in the following manner: 1) film composition, 2) deposition rate and 3) film contamination. Quanititative analyses of atomic concentration and film thickness were performed and are reported here for laser deposited compound films. The results for laser evaporated mixtures are then compared to theoretical estimates based on three models for evaporation. The results of qualitative chemical and physical analyses of film contamination are reported for both elemental and compound films. Finally, the potential for practical utilization of this technique for general purpose vacuum deposition of thin films is discussed.

Film Composition and Deposition Rates

The results of stoichiometry determinations are based on reduced spectroscopic data contained in the tables which follow. Table IV.1 contains RBS peak areas for molybdenum and silicon for each of the compound films deposited by laser evaporation. Table IV.2. contains the average peak to peak heights of differentiated Auger spectra. Specifically, the 186 eV MNN Auger molybdenum transition and the 1619 eV KLL Auger silicon transition intensities are reported for each of the compound films and for the previously characterized molybdenum disilicide film[29,30] used as a standard reference. Table IV.3. is comprised of average peak areas expressed in kcounts from MgKα X-ray photoelectron spectra. The reported values correspond to molybdenum $3p_{1/2}$, $3p_{3/2}$ and $3d_{5/2}$ and silicon 2s and 2p electron binding energies for each of the laser deposited films and for the reference silicide.

The collective results of the quantitative analyses performed by three different methods are summarized in Table IV.4. The mole fraction of molybdenum is given for each compound film and classified by method of quantitative analysis. The results are further sub-classified according the focusing method and laser power density used to produce the films. The results from all three analytical techniques are in close agreement (with one exception--ESCA result for sample #5 in Tables IV.3. and IV.4.). In each case silicon was preferentially vaporized, reguardless of laser power density.

The composition of the molybdenum silicide films deposited by pulsed laser evaporation of molybdenum-silicon mixtures are in close agreement with film stoichiometries computed on the basis of models which assume surface ablation of the target particles. The computed film stoichiometries, expressed as mole fractions of molybdenum, are reported for three theoretical evaporation fluxes for each target composition in Table IV.5.

The value listed in the second column is obtained from the equilibrium model and the Hertz-Knudsen-Lanngmuir equation. The equilibrium model assumes that each particle is raised to the

Table IV.1 RBS Peak Areas

$$N_{Si}/N_{Mo} = 9(A_{Si,gross}/A_{mo,net})$$

No.	$X_{Mo,T}$	$A_{Si,gross}$	$A_{Mo,net}$	$X_{Mo,F}$
4	0.33	1339	730	0.057
5	0.69	2350	4300	0.17
6	0.69	5753	10193	0.16
7	0.33	4876	2787	0.060
8	*0.33	8890	3444	0.041
9F	*0.33	1001	460	0.049
9R	*0.33	1527	619	0.043

*Molybdenum disilicide targets

Table IV.2. AES Peak-to-Peak Heights from Differentiated Spectra

$$N_{Si}/N_{Mo} = 1.6(I_{Si}/I_{Mo})$$

No.	$X_{Mo,T}$	I_{Si}	I_{Mo}	$X_{Mo,F}$
4	0.33	107	16	0.085
5	0.69	103	68	0.29
6	0.69	107	50	0.22
7	0.33	105	22	0.11
8	*0.33	104	15	0.083
9F	*0.33	104	13	0.072
9R	*0.33	106	12	0.066

*Molybdenum disilicide target

Table IV.3. ESCA Peak Areas

$$R_i = (2(A_{Si}/A_{Si,ref})(A_{Mo,ref}/A_{Mo}) + 1)^{-1} = X_{Mo,F}$$

$R_1 = Mo_{3p(1/2)}/Si_{2s}$; $R_2 = Mo_{3p(1/2)}/Si_{2p}$

$R_3 = Mo_{3p(3/2)}/Si_{2s}$; $R_4 = Mo_{3p(3/2)}/Si_{2p}$

$R_5 = Mo_{3d(5/2)}/Si_{2s}$; $R_6 = Mo_{3d(5/2)}/Si_{2p}$

No.	$X_{Mo,T}$	R_1	R_2	R_3	R_4	R_5	R_6	$\langle X_{Mo,F} \rangle$
4	0.33	**	**	0.052	0.041	0.052	0.041	0.057
5	0.69	0.59	0.70	0.38	0.53	0.62	0.34	0.53
6	0.69	0.18	0.19	0.18	0.19	0.20	0.19	0.19
7	0.33	0.060	0.061	0.080	0.061	0.062	0.080	0.067
8	*0.33	0.062	0.068	0.079	0.064	0.071	0.083	0.071
9F	*0.33	0.058	0.072	0.056	0.059	0.073	0.057	0.063
9R	*0.33	0.050	0.058	0.061	0.053	0.061	0.064	0.058

*Molybdenum disilicide target

Table IV.4. Summary of Quantitative Compositional Analysis

	$X_{Mo,T}$	$X_{Mo,F}$			
No		RBS	AES	ESCA	Scheme*
4	0.33	0.057	0.085	0.057	II
5	0.69	0.17	0.29	0.53	II
6	0.69	0.16	0.22	0.19	I
7	0.33	0.060	0.11	0.067	I
8	**0.33	0.041	0.083	0.071	I
9F	**0.33	0.049	0.072	0.063	II
9R	**0.33	0.043	0.066	0.058	II

*Refers to optical schemes I and II illustrated in figs. II.10. and II.11 respectively.

**Molybdenum disilicide targets

Table IV.5. Calculated Film Compositions

$X^{*}_{Mo,T}$	$X_{Mo,F}$ HKL	$X_{Mo,F}$ Quasi-Equilibrium			$X_{Mo,F}$ Plasma
		10^6 W/cm^2	10^7 W/cm^2	10^8 W/cm^2	10^9 W/cm^2
0.33	0.050	0.066	0.066	0.066	0.0600
0.69	0.17	0.24	0.24	0.23	0.20

---

[*] For molybdenum-silicon mixtures only

temperature at which its vapor pressure is equal to the ambient pressure. The third, fourth and fifth columns are computed using the low temperature quasi-stationary model. This quasi-equilibrium model is valid for incident laser power densities $\lesssim 10^8 \mathrm{W/cm^2}$ and assumes an adiabatic expansion of the vapor. The final column is based on the plasma generation model for power densities $\gtrsim 10^9 \mathrm{W/cm^2}$. Here it is assumed that the optical thickness for the ionized vapor is constant. The compositions are written as mole fraction of molybdenum and are calculated using the known specific surface area and the aforementioned theoretical evaporation fluxes.

Results of Auger depth profiling analysis are listed in Table IV.6. The time for sputtering through the films τ_s, the effective sputtering rate ξ_s, the number of laser pulses required to produce the films n_p and the effective deposition rate Γ_{eff} (Angstroms per pulse) where

$$\Gamma_{eff} = \tau_s \cdot \xi_s \cdot (n_p)^{-1} \qquad \text{IV.1.}$$

are given in the first four columns and the actual deposition rate Γ_d (Angstroms per second) listed in the final column is given by

$$\Gamma_d = \tau_s \cdot \xi_s \cdot (\Sigma\tau_p)^{-1} \qquad \text{IV.2}$$

where $\Sigma\tau_p$ is the sum of the pulse times.

Table IV.6. Film Thickness and Deposition Rate Determinations

Source to substrate distance of 3cm.

No.	τ_s min	ξ_s Å/min	n_p	Γ_{eff} Å/pulse	d Å	$\Sigma\tau_p$ sec	Γ_d Å/sec
4	1.67	80	1000	0.13	133	$2.5X10^{-4}$	$5.3X10^{5}$
5	0.40	80	500	0.06	32	$1.3X10^{-4}$	$2.6X10^{5}$
6	4.50	80	4000	0.09	360	$1.0X10^{-3}$	$3.6X10^{5}$
7	3.00	80	3000	0.08	240	$7.5X10^{-4}$	$3.2X10^{5}$
8	10.00	80	7000	0.11	800	$1.8X10^{-3}$	$4.6X10^{5}$
9F	0.6	80	500	0.13	64	$1.3X10^{-4}$	$5.1X10^{5}$
9R	0.8	80	500	0.10	48	$1.3X10^{-4}$	$3.8X10^{5}$

Film Contamination

Two types of film contamination which may occur during thin film deposition are of interest. The first, chemical contamination, is common to low and high vacuum deposition processes. The second, contamination in the form of solid debris is typical for laser evaporated thin films.

The results of in situ Auger analyses reveals qualitative information concerning the sources of chemical contamination. Figures II.17.-II.19. are a series of Auger spectra recorded in the following manner: The first spectrum was that recorded for the as inserted gallium arsenide substrate. The second spectrum was recorded following pulsed laser cleaning of the substrate at an ambient pressure of 5×10^{-10}torr. And the third spectrum was recorded immediately following 200 pulses on a molybdenum-silicon target mixture. The reemergence of Auger signals at 272 eV and 510 eV indicates carbon and oxygen contamination, respectively. The source of the contamination is most likely the target particles themselves. Additional post-deposition analysis indicates that the oxygen and carbon contamination is incorporated throughout the films.

The results of scanning electron microscopic analysis clearly shows that samples mounted in the rearward hemisphere along the direction of the laser beam have many times fewer debris particles (figures IV.1. and IV.2). The relatively small size of the debris arriving at rearward mounted specimens (fig IV.2.) indicates that debris moving in the rearward direction may be caused by explosions of large target particles.

Conclusions and Considerations for Future Work

The results of the previously described experiments demonstrate that defect-free, compositional films may be produced by pulsed laser irradiation of free-falling particles. This technique affords an fine control of an important deposition parameter which is surface area. The unique experimental geometry creates the potential for evaporation of multiple species from either a single point source (stationary focus) or a single ring source (relative motion of the focus and substrate) while maintaining high compositional accuracy. The composition of the resulting films are infinitely adjustable according to relative weights and relative specific surface areas of the target constituents.

The single most important refinement required for this technique is a reduction in the target particle size. For a decrease in the mean particle radius of an order of magnitude the attainable deposition rates should increase by at least a

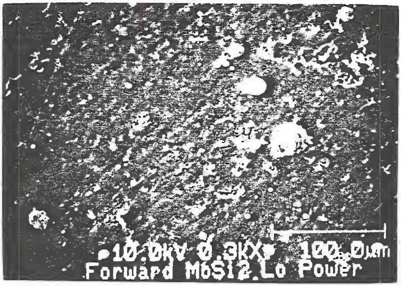

Fig. IV.1. SEM photograph of specimen mounted in the forward hemisphere along the direction of the laser beam

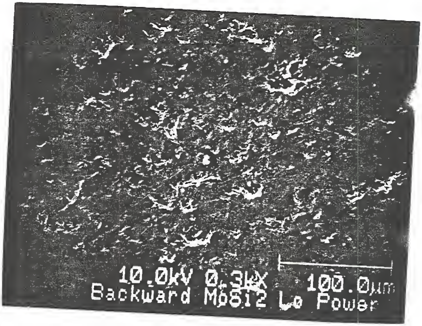

Fig. IV.2. SEM photograph of specimen mounted in the rearward hemisphere along the direction of the laser beam

corresponding order of magnitude. The effective deposition rates observed in these experiments are low for practical utilization of this technique. This is due to the extremely low duty cycle of the available laser (ca. 10^{-4}%) At a repetition rate of 1 pulse per second, the achievable, overall deposition rates are 10 to 100 times lower than conventional evaporation methods. Commercial lasers capable of delivering the same power densities used in this study at 50 to 100 times the repetition are available.[38] If such a laser were used to evaporate particles having mean particle diameters of 0.1 μm, the effective deposition rates attainable are as much as 100 times as great as those of conventional methods. Furthermore, the film thickness can be controlled with submonolayer accuracy. Smaller particles would tend to improve film qualities in at least three additional ways: 1) The increased homogeneity of the target resulting from finer particles should increase film homogeneity. 2) The decreased particle size should increase the accuracy with which composition can be controlled (for instance a doped film might be prepared from a target mixture in which the dopant concentration could be gravimetrically introduced with ppb accuracy) And 3) If sub-micron sized particles are used for targets, any debris which might arrive at the substrate would not produce a catastrophic flaw for most microelectronic applications.

Finally, the observation of enhanced electromagnetic processes on metallic surfaces[39,40] indicates that photon absorption by surface plasmons may be optimized by proper selection of particle size distributions. In a review of Surface Enhanced Raman Scattering (SERS), Wokaun writes :"Localized surface plasmons on metallic particles appear to be particularly efficient in providing strong amplification of optical fields at their surface."[40] If a metal particle is excited by light of the frequency at which the dipolar surface charge distribution would relax in an oscillatory manner it absorbs maximum power.[40] The observed Raman signal to noise enhancement, which is attributed mainly to this resonant absobtion, is reportedly as great as 10^6 for pyridine on silver spheres. It is thus likely that the improvements in evaporation rates for most metals and metalloids due to enhanced resonant absorption would exceed that predicted solely on the basis of specific surface area considerations.

APPENDIX A
REDUCING APERTURE

As previously explained, the reducing aperture (MA fig. II.11.) was provided to prevent film contamination from occurring by the desorbtion of surface contaminants on the powder curtain generator. A third focusing method (using an optical arrangement similar to that depicted in fig. II.13. which was attempted and subsequently discarded) employed a concave mirror to achieve the same end. Rutherford backscattering (RBS) and AES revealed large ammounts of gold incorperation in the films. The energy density incident on the internal focusing mirror was thus necessarily reduced to avoid similar gold incorperation in subsequent experiments.

The reduction of power density incident on the internal gold mirror was thus accomplished by using a thermal paper mask (MA; fig.11.). The power density calculation for optical scheme II thus included an energy loss term which was incorporated in equation II.2. as φ_A. The value of φ_A is taken as zero for optical scheme I. For optical scheme II it is computed in the following manner:

$$\phi_A = \frac{\text{Area of the mask opening}}{\text{Area of the unmasked beam}} \qquad \text{A.1.}$$

or

$$\phi_A = \frac{(d_A/2)^2}{(\phi_B/2)^2} \qquad \text{A.2.}$$

APPENDIX B
THERMOPHYSICAL DATA

Vapor pressure data taken from the JANAF tables[37] were used in order to evaluate sublimation temperatures at the ambient pressure of the deposition vessel. The values for T in equations III.3 and III.4 were determined from log K_p values assuming a monatomic vapor in equilibrium with the solid. In the case of silicon, the partial pressures of the dimer and trimer were calculated and found to be insignificant at the temperature ranges of interest. The resulting evaporation flux for silicon was thus computed on the basis of a monatomic vapor.

The preexponential factor A discussed in the next appendix and found in equation III.10. was likewise computed from JANAF[37] vapor pressure data. The following tables give the vapor pressures of silicon, molybdenum, tantalum and tungsten as a function of temperature over the temperature range of interest. Also included are the values for (ρ_s/p_s) and $\ln(\rho_s/p_s)$ for these elements over the same temperature range. Finally, the values of A computed for silicon, molybdenum, tantalum and tungsten are provided.

Table B.1. Thermophysical Data for Molybdenum

$T(K)$	p(atm)	ρ_s/p_s	$\ln(\rho_s/p_s)$	A
1000	2.7782E-27	1.1540E-09	-6.7792E01	1.7222E04
1100	3.6655E-24	1.0491E-09	-6.0739E01	
1200	1.4603E-21	9.6167E-10	-5.4877E01	
1300	2.3157E-19	8.8769E-10	-4.9927E01	
1400	1.7808E-17	8.2429E-10	-4.5697E01	
1500	7.6755E-16	7.6933E-10	-4.2042E01	
1600	2.0667E-14	7.2125E-10	-3.8852E01	
1700	3.7773E-13	6.7882E-10	-3.6046E01	
1800	4.9990E-12	6.4111E-10	-3.3560E01	
1900	5.0409E-11	6.0737E-10	-3.1344E01	
2000	4.0344E-10	5.7700E-10	-2.9355E01	
2100	2.6486E-09	5.4952E-10	-2.6320E01	

Table B.2. Thermophysical Data for Silicon

$$p_{tot} = p_{Si} + p_{Si_2} +\cdot p_{Si_3}$$

T(K)	p_{tot}	p_{Si}/p_{tot}	p_{Si}	ρ_s/p_s	$\ln\rho_s/p_s$
400	8.5842E-52	1.0000E-00	8.8584E-52	1.1260E-09	-1.6975E02
500	4.8521E-40	1.0000E-00	4.8521E-40	8.4452E-10	-1.2465E02
600	3.3170E-32	1.0000E-00	3.3170E-32	6.7562E-10	-9.7766E01
700	1.3093E-26	1.0000E-00	1.3093E-26	5.6302E-10	-7.9885E01
800	2.0619E-22	1.0000E-00	2.0619E-22	4.8259E-10	-6.7147E01
900	3.7912E-19	1.0000E-00	3.7912E-19	4.2226E-10	-5.7618E01
1000	1.5502E-16	9.9999E-01	1.5502E-16	3.7534E-10	-5.0230E01
1100	2.1240E-14	9.9997E-01	2.1240E-14	3.3781E-10	-4.4336E01
1200	1.2818E-12	9.9989E-01	1.2817E-12	3.0710E-10	-3.9528E01
1300	4.1174E-11	9.9968E-01	4.1161E-11	2.8151E-10	-3.5534E01
1400	8.0592E-10	9.9918E-01	8.0526E-10	2.5985E-10	-3.2167E01
1500	1.0617E-08	9.9814E-01	1.0597E-08	2.4129E-10	-2.9291E01

A = 9.7136E03

Table B.3. Thermophysical Data for Tantalum

T(K)	p(atm)	ρ_s/p_s	$\ln(\rho_s/p_s)$	A
1500	1.4000E-20	2.8832E-09	-5.2238E01	8.8976E03
2000	8.9000E-14	2.1624E-09	-3.6860E01	
2200	6.4000E-12	1.9658E-09	-3.2681E01	
2400	2.2086E-10	1.8020E-09	-2.9230E01	
2600	4.6000E-09	1.6634E-09	-2.6270E01	
2800	6.1100E-08	1.5445E-09	-2.3758E01	
3000	5.7400E-07	1.4416E-09	-2.1587E01	

Table B.4. Thermophysical Data for Tungsten

T(K)	p(atm)	ρ_s/p_s	$\ln(\rho_s/p_s)$	A
1600	5.7468E-21	1.3821E-09	-5.3175E01	3.3776E04
1700	2.6071E-19	1.3008E-09	-4.9424E01	
1800	7.7414E-18	1.2285E-09	-4.6091E01	
1900	1.6086E-16	1.1638E-09	-4.3110E01	
2000	2.4679E-15	1.1057E-09	-4.0430E01	
2100	2.9192E-14	1.0530E-09	-3.8007E01	
2200	2.7584E-13	1.0051E-09	-3.5806E01	
2300	2.1441E-12	9.6143E-10	-3.3801E01	
2400	1.4048E-11	9.2138E-10	-3.1964E01	

APPENDIX C
CLAUSIUS DERIVATION

The calculation of the mass evaporation flux for the low temperature laser heating model is completely described by Krokin.[18] The reader is refered to this paper for the full derivation of equations III.9 and III.10.. Two statements should be made here which would help to clarify the cited derivation. First, a relation between saturation vapor pressure p_s and density ρ_s is given:

$$\rho_s = A\exp(-U\rho_s/p_s) \qquad \text{C.1. (equation 20 in ref. 18)}$$

which is a form of the Clausius equation for an ideal gas. The preexponential term A is an important parameter in the computation of mass evaporation fluxes. The following derivation demonstrates the equivalence of the integrated Clausius equation and equation C.1. From this result the required method for obtaining A may be seen.

The Clausius equation is written:

$$\frac{dp}{dT} = \frac{\Delta H}{T\Delta V} \qquad \text{C.2.}$$

were H is enthalpy, p is pressure, T is absolute temperature and V is volume.

But $$\Delta\bar{V} = \bar{V}_g = 1/\rho_s \qquad \text{C.3.}$$

hence $$\frac{dp}{dT} = \frac{M \cdot p \cdot \Delta\bar{H}}{RT^2} \qquad \text{C.3.}$$

and $$\frac{dp}{p} = \frac{M\Delta\bar{H}}{RT^2}\, dT \qquad \text{C.4.}$$

if the ideal gas equation of state is assumed. The following substitution for saturated pressure may be made:

$$\rho_s = Mp/RT \qquad \text{C.5}$$

Equation C.4. may thus be written in terms of saturated vapor density instead of pressure as follows:

$$\frac{d\rho}{\rho} = \frac{M\Delta\bar{H}}{RT^2}\, dT \qquad \text{C.6.}$$

If equation C.6 is integrated with no integration limits the following result is obtained:

$$\ln\rho_s = -M\Delta\bar{H}/(RT) + C_1 \qquad \text{C.7.}$$

Again the ideal gas equation of state may be invoked:

$$\frac{RT}{M} = p_s\bar{V} = \frac{p_s}{\rho_s} \qquad \text{C.8.}$$

which gives:

$$\ln\rho_s = -U\rho_s/p_s + C \qquad \text{C.9.}$$

where U is the specific enthapy of sublimation. Finally:

$$\rho_s = e^{C_1}\cdot\exp(-U\rho_s/p_s) \qquad \text{C.10.}$$

where the preexponential factor e^{C_1} is A of equation C.1.

To obtain A then, it is necessary to obtain the intercept of the line plotted for $\ln\rho_s$ versus ρ_s/p_s. These values were obtained from the JANAF tables[37] from log K_p data over the temperature range of interest, where

$$\ln\left[\frac{M\exp(2.303\cdot\log K_p)}{RT}\right] = \ln(\rho_s) \qquad \text{C.11.}$$

and $$\rho_s/p_s = M/(RT) \qquad \text{C.12.}$$

The values obtained from equations C.11. and C.12 along with the values calculated for the preexponential factor A are given in the preceeding Appendix for silicon, molybdenum, tantalum, and tungsten.

Secondly, it should be explicitly stated that solutions to equations 23a, 23b, and 24a through 24c of the Krokhin[18] derivation must be obtained by an iterative technique. The method used to obtain λ_2 and λ_1 of equations III.9 and III.10. (23a and 23b of the cited derivation) is found in the following Appendix.

APPENDIX D
BASIC PROGRAM

The following BASIC program was used to iteratively solve equation III.10. for the parameter λ_2. The parameter λ_1 of equation III.9 could then be found using this value for λ_2.

The physical properties of the effluent vapor such as: velocity, pressure, density and temperature could then be solved using relationships developed by Krokin.[18] (equations 25a-25e in his work.)

Furthermore, the velocity of the ablation wave through the solid could be calculated from λ_2 in the following manner:

$$D = \frac{q_1}{\rho_o U[1+(\gamma-1)^2\lambda_2/2(\gamma+1)]} \qquad \text{D.1}$$

The mass evaporation flux could then be calculated as:

$$\Gamma_m = \rho_o \cdot D \qquad \text{D.2}$$

In the next appendix (Appendix E) the mass evaporation rates and the physical properties of the effluent vapor are reported for three different incident laser power densities, for silicon, molybdenum and two other refractory metals, tungsten and tantalum.

```
 5 REM input known physical constants
 7 REM
 8 REM
10 PRINT "ENTER A TEST (preexponetial factor from Clausius)
20 INPUT Z
30 PRINT "ENTER U (specific energy of sublm. erg/g)
40 INPUT U
50 PRINT "ENTER D (density of solid g/cm^3)
60 INPUT D
70 print "ENTER GAW (gram atomic weight)
80 INPUT A0
81 REM
82 REM laser power densities preselected for
83 REM three orders of magnitude
84 REM
85 REM
90    FOR I = 13 TO 15 '1 to 100 MW/square cm
100 Q = 10^I 'Q is power density
110 N = (Q/D)*(1/(U^1.5)) 'N is eta in text
111 REM
112 REM
113 REM iterative solution of lambda 2 with an
114 REM initial guess >0 but <lamda 2
115 REM for example 1 iteration times
116 REM are not long
117 REM
118 REM
120 PRINT "ENTER L (initial iteration value lamda 2)
130 INPUT L
140 Z1=Z/D 'ratio of preexponential term to density
150 A1 = -1*LOG(N/Z1)
160 L2 = 26.66666/SQR(LOG((0.011719*L^3 +0.09375*L))+A1)
170 PRINT L,L2
180 T = (L2-L)*10000 'convergence test to 5 sig. fig.
190 IF T<1 GOTO 220
200 L = (L2-L)/2 + L 'next iteration
210 GOTO 160
220 PRINT "L2 CONVERGED=";L2 'converges to this value
221 REM
222 REM
223 REM lambda 2 has converged and properties
224 REM of the vapor may be calculated
225 REM
226 REM
230 B = 26.66666
240 B1 = LOG((0.011719*L^3)+(0.09375*L))
250 B2 = 1/(1+(0.0833333*L^2))
251 REM
```

```
252 REM
253 REM from the three "B" terms all physical
254 REM properties of the vapor may be calculated
255 REM
256 REM
257 REM L1 is lambda 1, P1 is the pressure of the
258 REM vapor V1 is the vapor velocity, P is the
259 REM vapor density, and T1 is the temperature
260 REM of the vapor
261 REM
262 REM D1 is the velocity of the evaporation wave
263 REM through the solid
264 REM
265 REM
266 1 = -1*B2*N
270 P1 =(B2*1.66666*Q/(0.666666*U^1.5))*(SQR(B)/L2)
280 V1 =(0.6666666*SQR(U)*L2)/(1.6666666*SQR(B))
290 P =(B2*L2*0.666666666*Q)/((2.7778*SQR(B)*SQR(U))*1.01E6)
300 T1 = A0*U*L2/(B*8.314E7)
310 D1 = B2*Q/(D*U)
311 REM
312 REM
313 REM calculation of the mass evaporation flux
314 REM by three methods to check the self consistency
315 REM of the model and the calculations
316 REM
317 REM
318 REM GAM is calculated from the density of the solid
319 REM and the velocity of the evaporation wave
320 REM
321 REM GAM1 is calculated from lambda 1, density of
322 REM the solid and the specific energy of sublimation
323 REM
324 REM GAM2 is calculated from the velocity and
325 REM pressure of the vapor
326 REM
327 REM
328 GAM = D*D1
330 GAM1 = L1*D*SQR(U)
340 GAM2 = P1*V1
341 REM
342 REM
343 REM print out the physical variables for one
344 REM laser power density
345 REM
346 REM
347 LPRINT "POWER DENSITY =";Q;"ergs/square cm/sec"
348 REM
```

```
349 REM the solution parameters: lambda 2, lambda 1,
350 REM B, B1, B2
351 REM
352 REM
353 PRINT "L2=";L2;"L1=";L1;"B=";B;"B1=";B1;"B2=";B2
360 LPRINT "L2=";L2;"L1=";L1;"B=";B;"B1=";B1;"B2=";B2
361 REM
362 REM
365 REM the physical properties of the vapor: pressure,
366 REM temperature, velocity and density
367 REM
368 REM the physical properties of the solid:
367 REM velocity of evaporation wave and density
368 REM
369 REM
370 PRINT "P1=";P1;"V1=";V1;"P=";P;"T1=";T1;"D1=";D1;"D=";D
380 LPRINT "P1=";P1;"V1=";V1;"P=";P;"T1=";T1;"D1=";D1;"D=";D
381 REM
382 REM
383 REM printout of mass evaporation fluxs
384 REM computed from three relations
385 REM as a check for intraconsistency
386 REM of model and iteration. The negative
387 REM value for gamma2 indicates direction
388 REM away from solid
389 REM
390 REM
391 PRINT "GAMMA1=";GAM;"GAMMA2=";GAM1;"GAMMA3=";GAM2
400 LPRINT "GAMMA1=";GAM;"GAMMA2=";GAM1;"GAMMA3=";GAM2
410 REM
411 REM
412 REM end of first calculation
413 REM
414 REM
500    NEXT I 'compute for next laser power density
505 REM
506 REM
510 END ' end of program
```

APPENDIX E
MASS EVAPORATION FLUXES

Table E.1. Physical Properties of the Effluent Vapors for Low Temperature Laser Heating.

X	q_1 W/cm^2	λ_2	λ_1	v_1 cm/sec	p_1 dynes/cm^2	ρ_1 g/cm^3	T_1 K	D cm/sec
Mo	10^6	6.2057	$-1.30\text{X}10^{-5}$	125897	2.59	$2.75\text{X}10^{-4}$	18421	3.395
Mo	10^7	6.5994	$-1.18\text{X}10^{-4}$	133886	25.05	$2.35\text{X}10^{-3}$	19590	30.873
Mo	10^8	7.0733	$-1.06\text{X}10^{-3}$	143502	240.40	$1.97\text{X}10^{-3}$	20997	276.475
Si	10^6	6.0982	$-1.63\text{X}10^{-5}$	189206	1.71	$8.04\text{X}10^{-5}$	12394	6.526
Si	10^7	6.4719	$-1.49\text{X}10^{-4}$	200799	16.56	$6.91\text{X}10^{-4}$	13153	59.573
Si	10^8	6.9188	$-1.34\text{X}10^{-3}$	214666	159.32	$5.82\text{X}10^{-3}$	14062	536.182
Ta	10^6	6.4287	$-1.74\text{X}10^{-5}$	103492	3.20	$5.03\text{X}10^{-4}$	22663	3.617
Ta	10^7	6.8668	$-1.57\text{X}10^{-4}$	110544	30.84	$4.25\text{X}10^{-3}$	24207	32.617
Ta	10^8	7.4009	$-1.39\text{X}10^{-3}$	119142	294.49	$3.49\text{X}10^{-2}$	26090	288.941
W	10^6	6.1925	$-1.24\text{X}10^{-5}$	103200	3.16	$4.99\text{X}10^{-4}$	23769	2.661
W	10^7	6.5838	$-1.13\text{X}10^{-4}$	109721	30.53	$4.27\text{X}10^{-3}$	25271	24.207
W	10^8	7.0544	$-1.01\text{X}10^{-3}$	117563	293.14	$3.57\text{X}10^{-2}$	27078	216.917

Table E.2. Mass Evaporation Fluxes for Low Temperature Laser Heating as Calculated by Equations D.1. and D.2.

q_1 W/cm^2	Γ_{Mo} $gcm^{-2}s^{-1}$	Γ_{Si} $gcm^{-2}s^{-1}$	Γ_{Ta} $gcm^{-2}s^{-1}$	Γ_{W} $gcm^{-2}s^{-1}$
10^6	34.63	15.21	52.10	51.49
10^7	314.90	138.80	469.68	468.41
10^8	2820.05	1249.30	4160.75	4197.34

REFERENCES

1. H. M. Smith and A. F. Turner, Appl. Opt. 4(1), 147 (1965).

2. R. Glang, Handook of Thin Film Technology, L. I. Maissel and R. Glang, eds. (McGraw-Hill Book Company, Inc., New York, 1970), Chap.11.

3. P. D. Zavitsanos and W. E. Sauer, J. Electrochem. Soc. 115, 109 (1968).

4. H. Schwartz and H. A. Tourtellotte, J. Vac. Sci. Technol., 6(1), 373 (1969).

5. C. Oali, V. Daneu, A. Orioli, and S. Riva-Sanseverino, Appl. Opt. 15(5), 1327 (1976).

6. G. Groh, J. Appl. Phys. 39, 5804 (1968).

7. V. S. Ban and D.A. Kramer, J. Mater. Sci. 5, 978 (1970).

8. G. Hass and J. B. Ramsey, Appl. Opt. 8, 1115 (1969).

9. C. E. Myers, G. A. Murray and R. J. Kematick, J. Electrochem Soc. 132(8), C361 (1985).

10. H. Schwartz, Laser Interaction and Related Phenomena, H. Schwartz and H. Hora, eds. (Plenum Press, New York, 1971), p. 71.

11. S. P. Murarka, Silicides for VLSI Applications (Academic Press, New York, 1982), pp. 115-116 and Chap. IV.

12. G. A. West, K. W. Beeson and A. Gupta, J. Vac. Sci. Technol. A, 3(6), 2278 (1985).

13. A. K. Ghosh, RCA Review 35, 279 (1974).

14. V. P. Veiko, Ya. A. Imas, A. N. Kokora, and M. N. Libenson, Sov. Phys. Tech. Phys. 12(10), 1410 (1968).

15. V. A. Batanov, F. V. Bunkin, A. M. Prokhorov, and V. B. Fedorov, Sov. Phys. JETP, 36(2), 311 (1973).

16. V. A. Komotskii, Sov. Phys. Tech. Phys., 16(1), 168 (1971).

17. J. F. Ready, J. Appl. Phys., 36(2), 462 (1965).

18. O. N. Krokhin, Laser Handbook, F. T. Arecchi and E. O. Schulz-Du Bois, eds. (North-Holland Publ. Co., New York, 1972), p. 1371.

19. G. J. Pert, Plasma Physics (Pergamon Press, Belfast, 1974), pp. 1051-1068.

20. T. P. Hughes, Plasmas and Laser Light (John Wiley and Sons, New York, 1975), Chaps. 8 and 9.

21. J. M. Poate, G. Foti, and D. C. Jacobson, Surface Modification and Alloying by Laser, Ion, and Electron Beams (Plenum Press, New York, 1983), Chap. 2.

22. H. Hora, Laser Interaction and Related Phenomena, H. Schwartz and H. Hora, eds. (Plenum Press, New York, 1971), p. 273.

23. R. T. Meyer, A. W. Lynch, and J. M. Freese, J. Chem. Phys., 77, 1083 (1973).

24. R. L. Baker, M. A. Covington, and G. M. Rosenblatt, High Temperature Materials Chemistry Symposium, Electro. Chem. Soc., 163rd Meeting, San Fransisco, CA, 1983.

25. J. F. O'Hanlon, A User's Guide to Vacuum Technology (John Wiley and Sons, New York, 1976).

26. G. A. Somorjai, Chemistry in Two Dimensions (Cornell University Press, Ithaca, N.Y., 1981), Chaps. 1,2, and 5.

27. R. Glang, R. A. Holmwood and J. A. Kurtz, Handook of Thin Film Technology, L. I. Maissel and R. Glang, eds. (McGraw-Hill Book Company, Inc., New York, 1970), Chap. 2.

28. G. M. Schrag and S. O. Colgate, J. Vac. Sci. Technol. A, 5(3), 388 (1987)

29. J. K. Truman, Master's Thesis, University of Florida (1984).

30. J. K. Truman and P. H. Holloway, J. Vac. Sci. Technol. A, 3(3), 992 (1985).

31. M. D. Sacks, Ceramic Bull., 63(12), 1510 (1984).

32. S. M. Bedair and H. P. Smith, Jr., J. Appl. Phys., 40(12), 4776 (1969).

33. D. M. Zehner and C. W. White, Appl. Phys. Lett. 36(1), 56 (1980)

34. W. P. Wresh, Master's Thesis, University of Florida (1987)

35. G. Foti, J. W. Mayer and E. Rimini, Ion Beam Handbook for Materials Analysis, S.U. Campisano, W. K. Chu, G. Foti, J. W. Mayer, M-A. Nicolet and E. Rimini, eds. (Academic Press, Inc., New York, 1977), Chap. 2.

36. P. W. Palmberg, G. E. Riach, R. E. Weber and N. C. MacDonald, Handbook of Auger Electron Spectroscopy, (Physical Electronics Industries, Inc., Edina, MN, 1972).

37. JANAF Thermochemical Tables (National Bureau of Standards, Washington, 1971), NSRDS-NBS No. 37

38. Lasers and Applications, 1987 Buying Guide, Agnes Dubberly, ed. (High Tech Publications, Torrence, CA, 1987).

39. J. A. Creighton, C. G. Blatchford and M. G. Albrecht, J. Chem. Soc., Faraday Trans. II, 75, 790 (1979).

40. A. Wokaun, Molec. Phys., 56(1), 1 (1985).

BIOGRAPHICAL SKETCH

Grant Michael Schrag was born in Kansas City, Missouri, on December 2, 1957. In 1964, his family moved to Atchison, Kansas, where he attended elementary and secondary school. Following after his mother, father and older sister, he enrolled at Eastern Nazarene College in Quincy, Massachusetts, where he received the B.S. degree in chemistry in August, 1980. Since September, 1980 he has been enrolled in the Graduate School of the University of Florida studying for the Ph.D. degree. During his graduate studies he has received Presidential recognition from the University of Florida, 1985, the University of Florida Department of Chemistry Proctor and Gamble Research Fellowship, 1985, and the University of Florida Department of Chemistry DuPont Teaching Award, 1984.

I certify that I have read this study and that in my opinion it conforms to acceptable standards of scholarly presentation and is fully adequate, in scope and quality, as a dissertation for the degree of Doctor of Philosophy.

Samuel O. Colgate

Samuel O. Colgate, Chairman
Associate Professor of Chemistry

I certify that I have read this study and that in my opinion it conforms to acceptable standards of scholarly presentation and is fully adequate, in scope and quality, as a dissertation for the degree of Doctor of Philosophy.

M. L. Muga

M. Luis Muga
Professor of Chemistry

I certify that I have read this study and that in my opinion it conforms to acceptable standards of scholarly presentation and is fully adequate, in scope and quality, as a dissertation for the degree of Doctor of Philosophy.

William Weltner

William Weltner
Professor of Chemistry

I certify that I have read this study and that in my opinion it conforms to acceptable standards of scholarly presentation and is fully adequate, in scope and quality, as a dissertation for the degree of Doctor of Philosophy.

Martin Vala

Martin Vala
Professor of Chemistry

I certify that I have read this study and that in my opinion it conforms to acceptable standards of scholarly presentation and is fully adequate, in scope and quality, as a dissertation for the degree of Doctor of Philosophy.

Thomas L. Bailey
Thomas Bailey
Professor of Physics

This dissertation was submitted to the Graduate Faculty of the Department of Chemistry in the College of Liberal Arts and Sciences and to the Graduate School and was accepted as partial fulfillment of the reqirements for the degree of Doctor of Philosophy

August, 1987

Dean, Graduate School